International Communications in Heat and Mass Transfer 130 (2022) 105815

Contents lists available at ScienceDirect

International Communications in Heat and Mass Transfer

journal homepage: www.elsevier.com/locate/ichmt

Transient melting flow of a NePCM comprising GNPs in a semi-elliptical latent heat thermal energy storage unit

Mohammad Shahabadi [a], Bader Alshuraiaan [b,*], Awatef Abidi [c,d,e], Obai Younis [f,g], Mohammad Ghalambaz [h,i], S.A.M. Mehryan [j,*]

[a] School of Aerospace and Mechanical Engineering, University of Oklahoma, Norman, OK 73019, United States of America
[b] Department of Mechanical Engineering, Kuwait University, 13060 Safat, Kuwait
[c] Physics Department, College of Sciences Abha, King Khalid University, Abha, City, 61421, Saudi Arabia
[d] Research Laboratory of Metrology and Energetic Systems, National Engineering School, Energetic Engineering Department, Monastir University, Monastir City 5000, Tunisia
[e] Higher School of Sciences and Technology of Hammam Sousse, Sousse University, Sousse City 4011, Tunisia
[f] Department of Mechanical Engineering, College of Engineering at Wadi Addwaser, Prince Sattam Bin Abdulaziz University, Saudi Arabia
[g] Department of Mechanical Engineering, Faculty of Engineering, University of Khartoum, Sudan
[h] Metamaterials for Mechanical, Biomechanical and Multiphysical Applications Research Group, Ton Duc Thang University, Ho Chi Minh City, Vietnam
[i] Faculty of Applied Sciences, Ton Duc Thang University, Ho Chi Minh City, Vietnam
[j] Young Researchers and Elite Club, Yasooj Branch, Islamic Azad University, Yasooj, Iran

ARTICLE INFO

Keywords:
Semi-elliptical LHTES unit
Melting flow
GNPs
Inclination angle
Aspect ratio

ABSTRACT

A cutting-edge achievement alleviating the shortage of energy sources and mitigating environmental pollution is latent heat thermal energy storage (LHTES). This system employs quality phase change materials (PCMs) to provide both large thermal capacity and slight temperature variation. This numerical work investigates the effects of structural parameters of a semi-elliptical LHTES unit, including aspect ratio (*AR*) and inclination angle (γ). In the semi-elliptical LHTES unit, heat is transferred from water as HTF to the PCM improved with graphite nanoplatelets (GNPs) through an interface copper wall. The investigation found that the melting time for $AR = 0.5$ decreases about 12% compared to that of $AR = 1.0$. Also, the LHTES unit of $AR = 0.5$ shows the highest power of the system, around 13.9% more than the unit having $AR = 1.0$. Furthermore, the temperature fluctuations are suppressed at lower *AR*s. Angular deviation of the system from the horizontal state is associated with an increase in the melting time, leading to a decrease in the unit power. It is seen that the unit of nano-plates mass fraction of $\varphi = 1.0\%$ has the highest power, 7.2% more than that of pure PCM.

1. Introduction

Thermal energy storage has gained considerable attention during recent years since it is an inevitable part of waste heat recovery systems and sustainable energy. Wind and solar energy are two promising clean energy sources. In these renewable applications, there is a time difference between energy generation and energy consumption. Thus, the thermal energy storage modules are required to store thermal energy and release it on demand [1]. The phase change materials (PCMs) are excellent candidates for thermal energy storage. PCMs can store/release a significant amount of latent heat energy at a constant temperature [2,3]. Therefore, compact thermal energy systems (TESs) could be designed using PCMs for renewable energy systems [4,5], waste heat recovery [6], and buildings energy [7,8] applications. Although PCMs can store/release a notable amount of thermal energy, their low thermal conductivity is a barrier in their practical applications [9,10]. For example, solar energy is available at its peak intensity at limited times; thus, a latent heat TES unit should store the excess solar heat in a short time. As a result, many researchers have focused on heat transfer enhancement techniques to improve the performance of the latent heat TESs.

One of the typical approaches for improving heat transfer in a TES module is using extended fins. The extended fins channel the heat inside the PCM material by construction mechanism and improve the heat transfer. Considering the fins, Tian et al. [11] examined the impact of

* Corresponding authors.
E-mail addresses: alshuraiaan@yahoo.com (B. Alshuraiaan), mohammad.ghalambaz@tdtu.edu.vn (M. Ghalambaz), alal171366244@gmail.com (S.A.M. Mehryan).

https://doi.org/10.1016/j.icheatmasstransfer.2021.105815

Available online 9 December 2021

Nomenclature

Latin symbols

a (cm)	radius of the semi-elliptical container in the x-direction
AR (a/b)	aspect ratio
A_{mush} (kg/m^3s)	mushy constant
b (cm)	radius of the semi-elliptical container in the y-direction
B	melting fraction of the liquid phase
C_p $(kJ/kg.K)$	constant pressure specific heat capacity
f_{b_i} (N/m^3)	buoyancy term
f_{m_i} (N/m^3)	momentum source
g (m/s^2)	gravity
h_{HTF} (mm)	height of the channel cross-section
i	ith coordinate
L (kJ/kg)	latent heat
p (Pa)	pressure
t (s)	time
T (K)	temperature field
th (mm)	thickness
v (m/s)	velocity component
x, y (m)	cartesian coordinates

Greek symbols

ρ (kg/m^3)	density
β $(1\ K^{-1})$	coefficient of thermal expansion
ΔT_{me} (K)	melting temperature window
λ $(W/m.K)$	thermal conductivity
μ $(Pa.s)$	dynamic viscosity
γ (rad)	inclination angle
φ	nano-plates mass fraction

Subscripts

HTF	heat transfer fluid
iw	interface wall
$lnepcm$	liquid state of the nano-enhanced phase change material
me	melting
$mush$	mushy zone
$snepcm$	solid state of the nano-enhanced phase change material
$nepcm$	nano-enhanced phase change material
0	initial conditions

Abbreviates

HTF	heat transfer fluid
$GNPs$	Graphite nanoplatelets
$LHTES$	latent heat thermal energy storage
MVF	normalized melting volume fraction
$NePCM$	nano-enhanced phase change material
pfp	phase-field parameter
PCM	Phase change material
POS (kJ/m)	power of energy storage unit
TES (kJ)	thermal energy systems

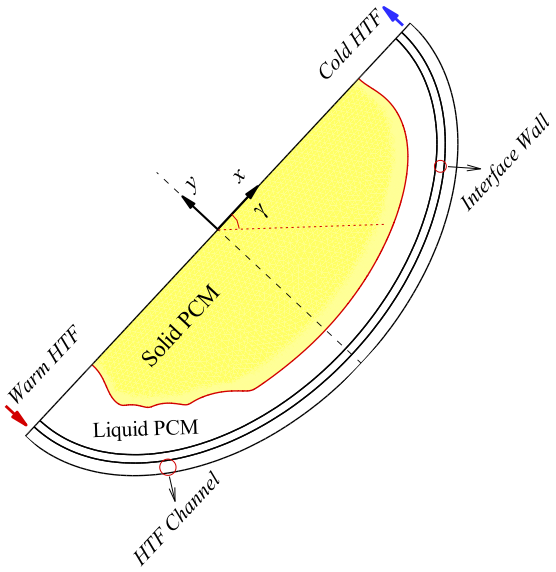

Fig. 1. Schematic view of the problem.

Table 1
Thermophysical properties of the HTF and interface wall [37,38].

Properties	ρ (kgm^{-1})	μ (Nsm^{-2})	C_p $(JkgK^{-1})$	λ $(Wm^{-1}\ K^{-1})$
HTF	993.73	0.705×10^{-3}	4178	0.623
Interface wall	8900	Not defined	386	401

using fins on the melting time and heat transfer behaviour of PCMs in a rectangular thermal energy storage enclosure. The outcomes showed that using copper, aluminum, carbon steel, and steel 302 fins reduce the charging time by 41.6%, 41.0%, 40.1% and, 37.2% compared with a no-fin case. However, the presence of fins reduces the stored energy per mass since the solid fins cannot store latent heat. Raj et al. [12] investigated the influence of fin configurations on the thermal behaviour of a TES module filled with solid-solid PCM. The impact of the fin's total number, base thickness, shape, and thickness on the charging/discharging cycle of the PCM module was investigated. The TES module was subjected to a constant heat flux of 10 W at 1200 s "on", 4800 s "off" duty cycles. The straight, triangular, and circular fins were studied, and the results showed that a triangular fin could show a good heat transfer performance with a mass reduction of 35% and 25% compared to circular and square fins. Arshad et al. [13] analyzed the finned heat sinks for cooling electronic components. The n-eicosane (PCM) was used to store the generated heat of electronic components. The PCM with low temperature keeps the heat sink base temperature at lower limits, and uniform melting is observed inside the finned heat sink. Bondareva and Sheremet [14] examined the melting heat transfer of PCMs in a finned copper heatsink for thermal control of radio equipment. The authors considered the natural convection effects in the liquid region. The results showed unsteady plumes of convection flows in the molten region. The cooling performance of the heatsink was under a significant influence of loading time and frequency.

Table 2
Thermophysical specifications of the NePCM samples at various loading of graphene nano-additives [36].

Characteristics		0 wt%	0.5 wt%	1 wt%	3 wt%
Thermal expansion coefficient, $(1\ K^{-1})$		10.18×10^{-4}	10.18×10^{-4}	10.08×10^{-4}	9.87×10^{-4}
Density (kgm^{-3})	solid	891.4	894.1	896.9	907.9
	liquid	821.6	824.3	826.9	837.6
Thermal conductivity $(Wm^{-1}\ K^{-1})$	solid	0.252	0.350	0.451	0.540
	liquid	0.159	0.180	0.260	0.320
Specific heat capacity $(Jkg^{-1}\ K^{-1})$	solid	2040	2020	1990	1910
	liquid	2360	2330	2300	2190
Latent heat $(kJkg^{-1})$		227.8	219.5	212.2	183.5
Dynamic viscosity $(mPa.s)$		13.23	23.45	59.5	194.01

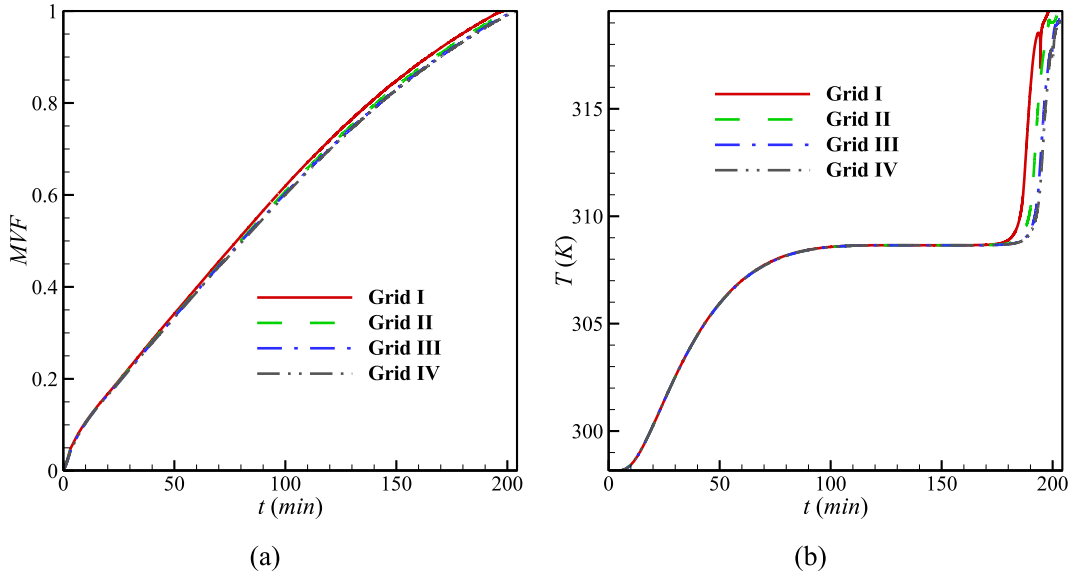

Fig. 2. Dependency of (a) the melted volume fraction and (b) temperature history at (0, $-b/2$) to the number of elements.

Table 3
Grid cases for the mesh dependency evaluation.

Grid number	Grid I	Grid II	Grid III	Grid IV
Number of elements	3926	5432	7124	8932
Running time	7 h, 58 min, and 27 s	12 h, 14 min, and 57 s	19 h, 56 min, and 23 s	22 h, 10 min, and 17 s

Some researchers utilized the metal foams filled with PCMs to improve the heat transfer performance of thermal energy storage modules. A composite of PCM-metal foam shows a high effective thermal conductivity and a good melting/releasing heat capability. However, the presence of a metal foam could suppress the natural convection flows in a liquid PCM and thus deteriorate the natural convection heat transfer mechanism. Sardari et al. [15] studied the impact of using metal foams on the charging time of a composite PCM-metal foam heat exchanger. The results showed that using metal foams could considerably reduce the melting time. The authors also found that a heat exchanger with a porosity of 97% could be used for domestic applications. Using metal foam could also improve the discharging process for air heat exchanger domestic applications [16]. Mahdi et al. [17] employed a cascade of metal foam-PCM composites for thermal storage heat exchangers. A heat exchanger made of several segments of different metal foams showed better performance than a single uniform layer of metal foam. However, using too many segments could not be recommended due to production limitations. Sardari et al. [18] examined the effect of porosity and pore density on the thermal performance of a latent heat TES module. They found that the variation of the foam porosity could change the melting time notably, while the pore density showed minimal impact on the melting time. The study of Li et al. [23] also demonstrates the effectiveness of using metal foams in TESs.

A novel approach to improve the heat transfer performance of PCM in latent heat TES modules is using nano-additives [19]. Dispersing nanoparticles in the PCM could enhance the thermal conductivity of the suspension and result in a nano-enhanced PCM [10,20]. Bondareva et al. [21] used alumina nanoparticles to enhance the melting heat transfer for cooling applications. Authors reported that using nanoparticles accelerated the melting heat transfer at the early stages of melting since all domains were in the solid state. However, as the melting advanced and the liquid region developed, the presence of nanoparticles reduced the strength of natural convection flows since a liquid containing nanoparticles shows a high viscosity. Ma et al. [22] investigated the influence of copper nanoparticles on the solidification of paraffin nano-enhanced

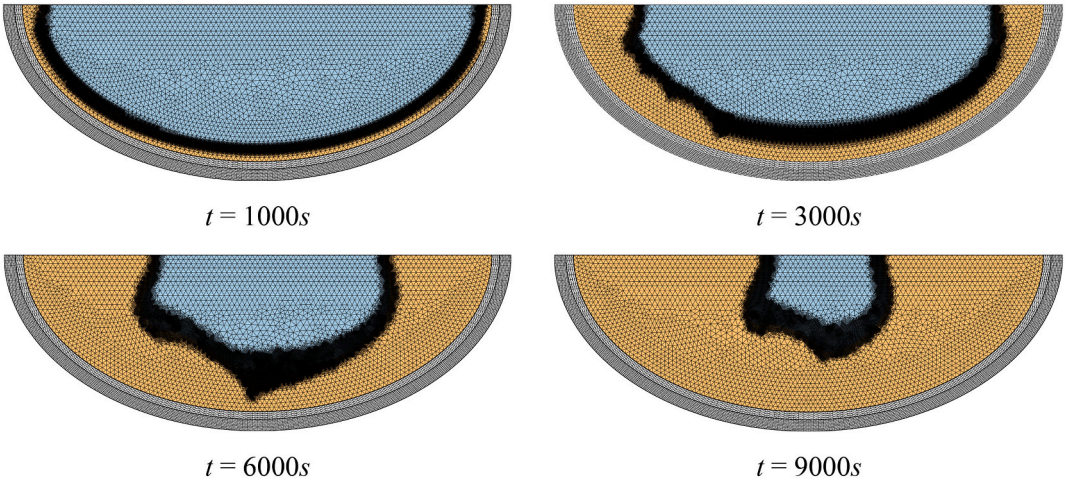

Fig. 3. Adaptive mesh history with $AR = 1.5$ for $\varphi = 0.5\%$, $\gamma = \pi/4$.

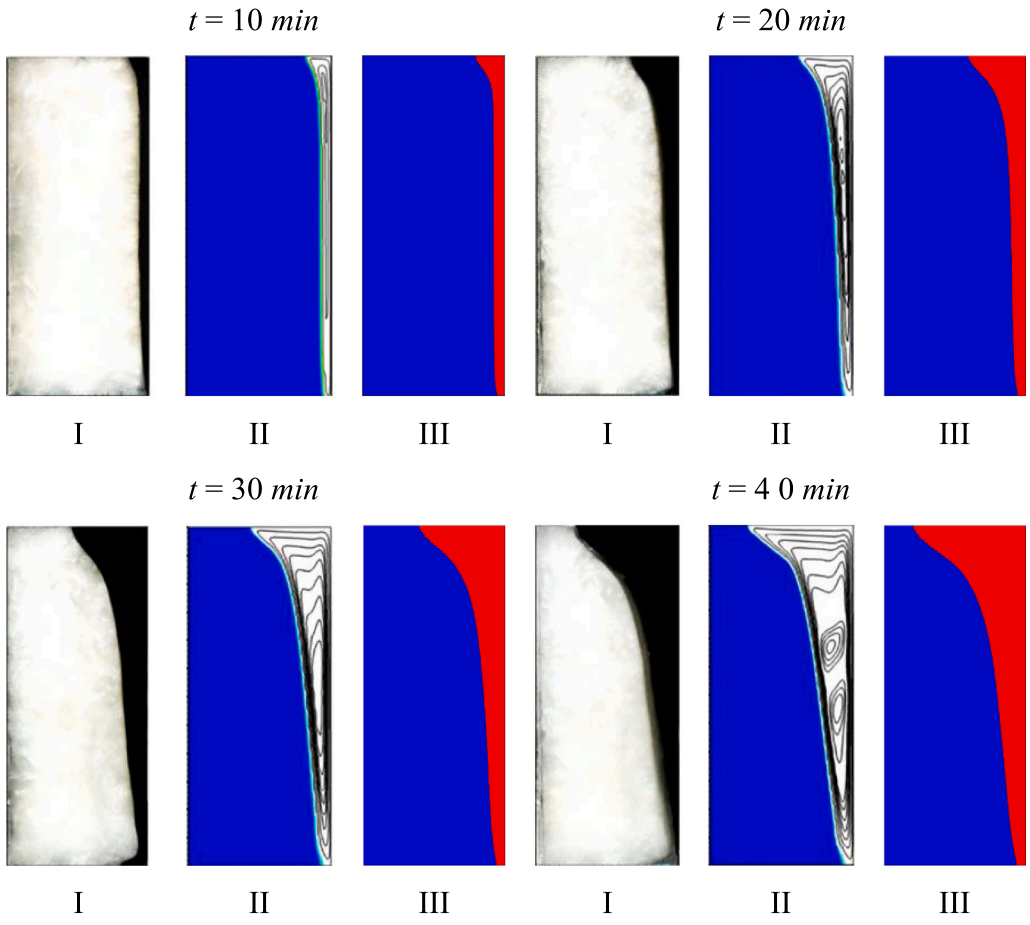

Fig. 4. Evaluation of the liquid fraction of the current work through the experimental and numerical results reported by Kamkari et al. [46]; I: experimental, II: numerical, and III: current work.

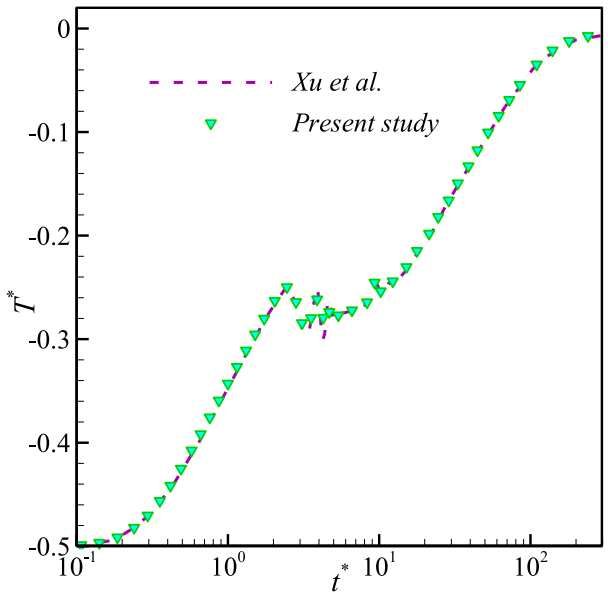

Fig. 5. Time history of the temperature of the Xu et al. [47] and the current model.

PCMs for domestic latent heat TESs. The copper nanoparticles improved the solidification heat transfer and were promising for solar energy storage systems. Li et al. [23] also reported the effectiveness of using nanoparticles in a shell and tube latent heat TES. Faraji [24] et al. utilized nano additives to improve the heat transfer of n-eicosane for cooling electronic components. Using 4%-Cu nanoparticles reduced the operating temperature of the electronic component by 4.69%. Bondareva et al. [25] studied the performance of a finned PCM unit affected by the tilted angle. They showed that dispersing the Al_2O_3 nano-additives to the paraffin wax can accelerate the melting process at any inclination of the system, consequently, reducing the melting time. Bondareva and Sheremet [26] investigated the possibility of using aluminum oxide nanoparticles inside a copper radiator filled with the n-octadecane as a PCM. They reported that the effectiveness of nano-additives on the performance of the radiator depends on the force of convective heat transfer. The literature review shows that the shape of a container is an important parameter that could notably affect the performance of a latent heat TES unit. The shape of an enclosure contributes to the temperature distribution and the flow of natural convection. Thus, some researchers focused on the shape of a PCM enclosure. Chu et al. [27] investigated the melting of PCM in an enclosure with wavy shape walls. The impact of the amplitude of the wavy wall was analyzed on the melting time. The results showed that the increase of the wavy-wall amplitude decreased the melting time by 22.66%. Sheikholeslami et al. [28] examined the solidification heat transfer in a wavy enclosure with V-shape fins. The results showed that the structure of the enclosure could influence the convection heat transfer and solidification time. Li et al. [29] studied discharging process of a latent heat TES unit made of a sinusoidal-wall shape enclosure. This study showed that the rise of the amplitude of the wall reduced the charging time by 44.9%. The phase change heat transfer in enclosures with annulus [30,31], rectangular [32–34], cylindrical [35], and spherical capsules have been examined in

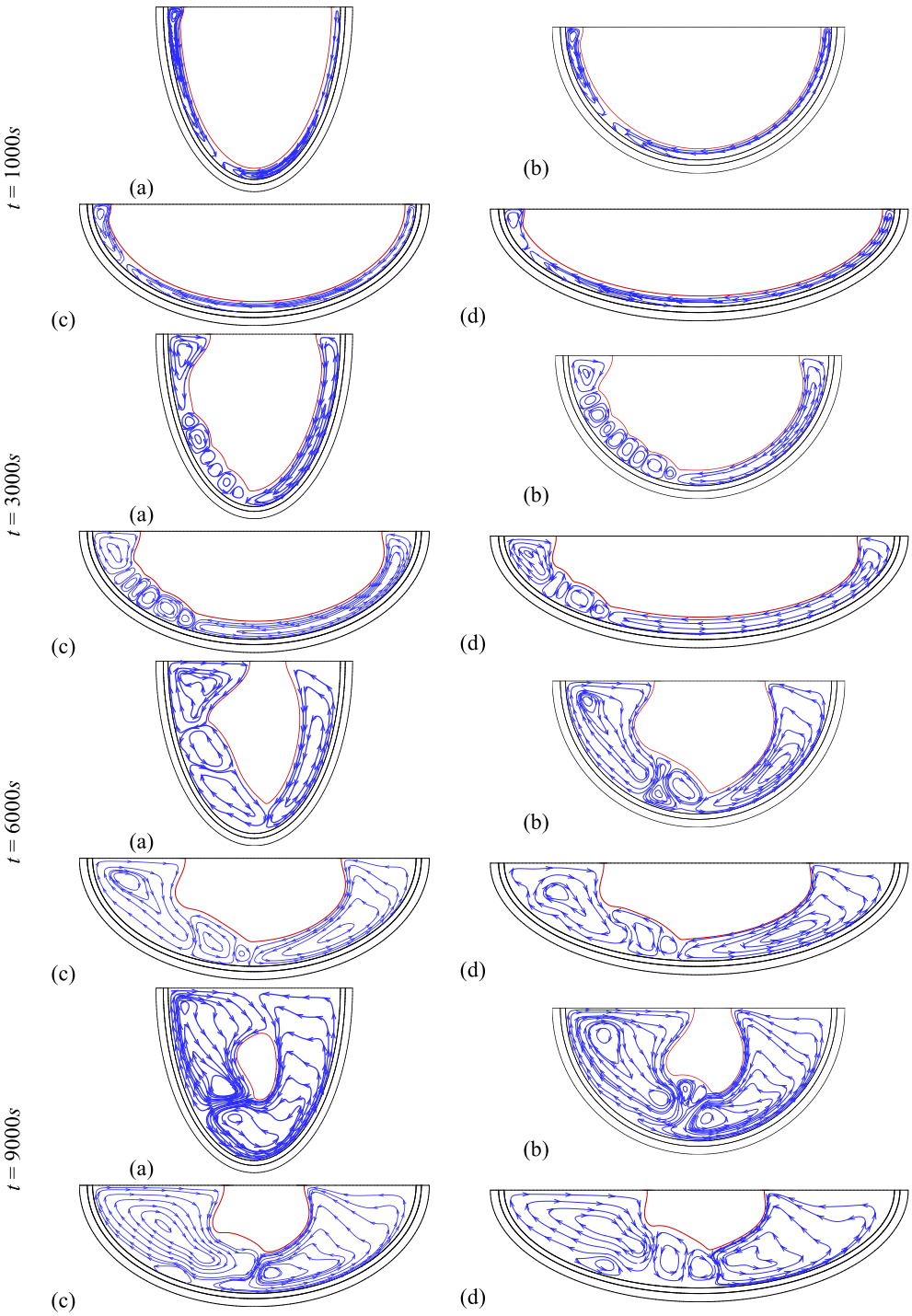

Fig. 6. Variations of Melted PCM domains and flow fields over time for (a): $AR = 0.5$, (b): $AR = 1.0$, (c): $AR = 1.5$, (d): $AR = 2.5$ at $\gamma = \pi/4$ and $\varphi = 0.5\%$.

recent studies. The results of these investigations highlight the significance of enclosure shapes on the thermal performance of latent heat TES units.

The literature review shows that using nanoparticles could improve the heat transfer performance of PCMs in various applications. Alumina and copper nanoparticles are widely utilized as nano additives. However, novel nano additives with excellent heat transfer characteristics, such as graphene nanoparticles, could improve the thermal conductivity of nano-enhanced PCMs notably. Moreover, the geometry of the latent heat TES module could impact the formation of natural convection flow in molten regions of the unit. The present study aims to examine the effectiveness of graphene nanoparticles in a semi-elliptical latent heat TES module.

2. Mathematical model

Fig. 1 illustrates the LHTES semi-elliptical system, saturated with a nano-enhanced phase change material. Since the dimension of the system perpendicular to the plane of paper is very large compared to the other two dimensions, the system can be considered two-dimensional. As shown, the semi-elliptical diameter has an inclination angle of γ relative to the x-axis. As depicted in Fig. 1, hot water as the heat transfer fluid (HTF) uniformly enters the channel and transfers some of its heat energy to the NePCM domain through the interface copper wall, leading

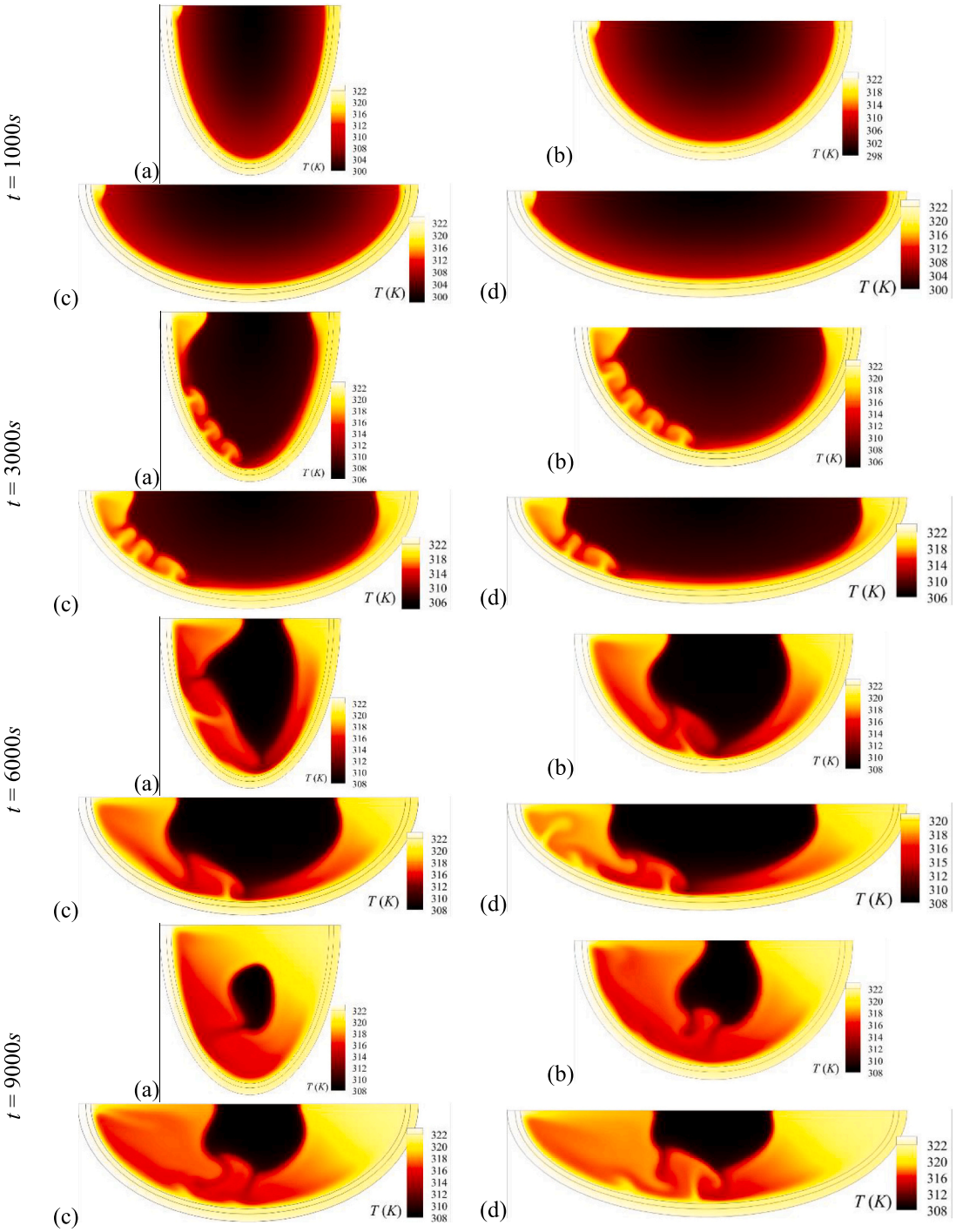

Fig. 7. Temperature fields over time for (a): $AR = 0.5$, (b): $AR = 1.0$, (c): $AR = 1.5$, (d): $AR = 2.5$ at $\gamma = \pi/4$ and $\varphi = 0.5\%$.

to the melting of the NePCM. It is worth noting that the velocity and temperature of the HTF entering the channel are 0.01 *m/s* and 323.15 K, respectively. Moreover, the initial temperature of the NePCM container is 298.15 K. The outer surface of the HTF channel and the surface of the NePCM along the *x*-direction are well insulated. The host PCM and dispersed nano-additives are 1-Tetradecanol and graphite nanoplatelets (GNPs), respectively. The thermophysical characteristics of the HTF, interface wall, and the NePCM are tabulated in Tables 1 and 2. It is noteworthy that in this study, thermophysical properties obtained experimentally are used for calculations of the NePCM [36]. The radii of the NePCM container are *a* and *b* in the *x* and *y* directions, respectively. The surface of the container in the *x*- *y* plane, as a constraint, is 78.54 mm^2 and the aspect ratio, i.e. *AR*, is *a*/*b*. The thickness of the interface wall, th_{iw}, is 2 *mm*, and the height of the channel cross-section, *h*, is 3 *mm*. To model the transient phase change flow of the NePCM the following assumptions are considered to be true; I) the volume change of the NePCM is disregarded while melting, II) GNPs are homogenously dispersed inside the host 1-Tetradecanol, III) GNPs do not experience any accumulation and settlement. IV) The Boussinesq linear approximation for applying the gravity-buoyancy term is valid. V) At the solid boundaries, the fluid has zero velocity relative to the boundary.

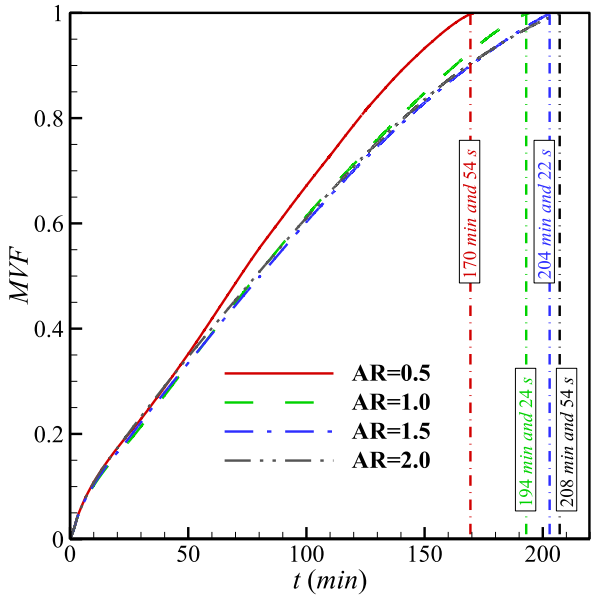

Fig. 8. Dependency of the *MVF* and the full melting time on the *AR* for $\gamma = \pi/4$ and $\varphi = 0.5\%$.

3. Governing equations and boundary conditions

3.1. Convective phase change heat transfer in NePCM

The enthalpy-porosity method along with a constant grid is employed to follow the phase change flow of the NePCM. Employing the above-considered assumptions, the controlling equations of the momentum and energy fields for the NePCM domain are as the following [25,39,40]:

I) Continuity equation

$$\frac{\partial v_i}{\partial x_i} = 0 \tag{1}$$

II) Momentum equations

$$\rho_{lnepcm}\left[\frac{\partial v_i}{\partial t} + v_j\frac{\partial v_i}{\partial x_j}\right] = -\frac{\partial p}{\partial x_i} + \mu_{lnepcm}\frac{\partial^2 v_i}{\partial x_j \partial x_j} + f_{b_i} + f_{m_i} \tag{2}$$

i of the equations is the ith coordinate so that $x_1 = x$ and $x_2 = y$. Also, $v_1 = u$ and $v_2 = v$. The velocity in the solid region tends to zero by using the momentum sinks, given by:

$$f_{m_i} = -\frac{A_{mush}(1 - B(T))^2}{B^3(T) + \varepsilon} v_i \tag{3}$$

A_{mush} is a constant value large enough ($A_{mush} = 5 \times 10^6 (kg/m^3 s)$) to ensure the vector velocity tends to zero when approaching the solid phase of the NePCM. Also, ε is a constant value small enough to avoid the denominator becoming 0 ($\varepsilon = 10^{-3}$). B (T) of the above-expressed equation, as a volume fraction of the melted liquid, is a ramp function, given by:

$$B(T) = \begin{cases} 0 & T < T_{me} - \Delta T_{me}/2 \\ \dfrac{T - T_{me}}{\Delta T_{me}} + \dfrac{1}{2} & T_{me} - \Delta T_{me}\Big/2 < T < T_{me} + \Delta T_{me}\Big/2 \\ 1 & T > T_{me} + \Delta T_{me}/2 \end{cases} \tag{4}$$

Also, the buoyancy terms, imposed on the NePCM domain, are:

$$f_{b_i} = -\rho_{lnepcm} g_i \beta_{lnepcm} = -\rho_{lnepcm} g \beta_{lnepcm} (sin\gamma, cos\gamma) \tag{5}$$

The controlling equation of energy conservation for the NePCM domain is as the following:

$$\rho_{nepcm} C_{p,nepcm}\frac{\partial T}{\partial t} + \rho_{lnepcm} C_{p,lnepcm} v_i \frac{\partial T}{\partial x_i} = \frac{\partial}{\partial x_i}\left(\lambda_{nepcm}\frac{\partial T}{\partial x_i}\right) - \rho_{snepcm} L_{nepcm}\frac{\partial B(T)}{\partial t} \tag{6}$$

in which,

$$\lambda_{nepcm}(T) = \lambda_{snepcm} + B(T)\left[\lambda_{lnepcm} - \lambda_{snepcm}\right] \tag{7a}$$

$$\rho_{nepcm}(T) = \rho_{snepcm} + B(T)\left[\rho_{lnepcm} - \rho_{snepcm}\right] \tag{7b}$$

$$\rho_{nepcm} C_{p,nepcm} = \rho_{snepcm} C_{p,snepcm} + B(T)\left[\rho_{lnepcm} C_{p,lnepcm} - \rho_{snepcm} C_{p,snepcm}\right] \tag{7c}$$

3.2. Forced convection heat transfer of HTF in channel

The HTF flowing inside the channel is assumed to be viscous,

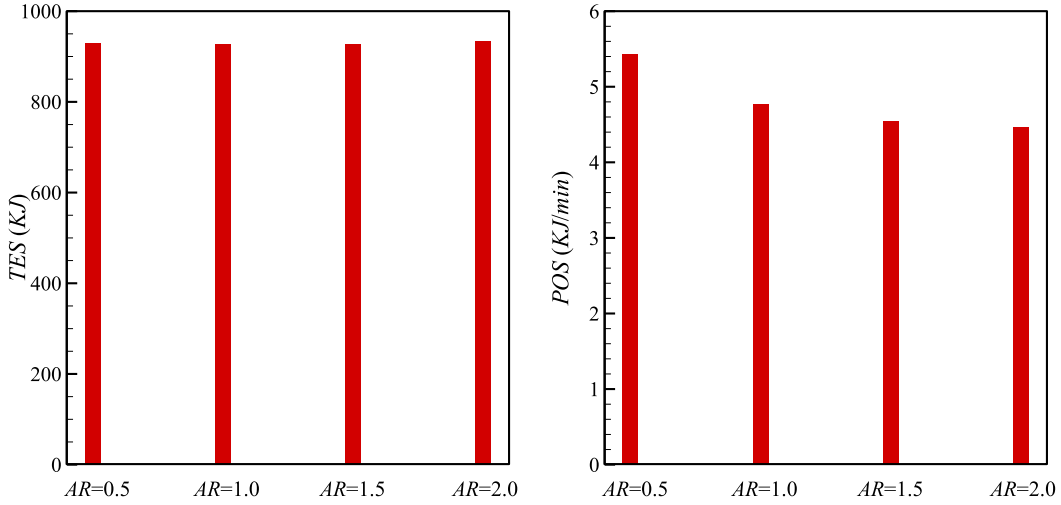

Fig. 9. Dependency of the *TES* and *POS* characteristics on the *AR* for $\gamma = \pi/4$ and $\varphi = 0.5\%$.

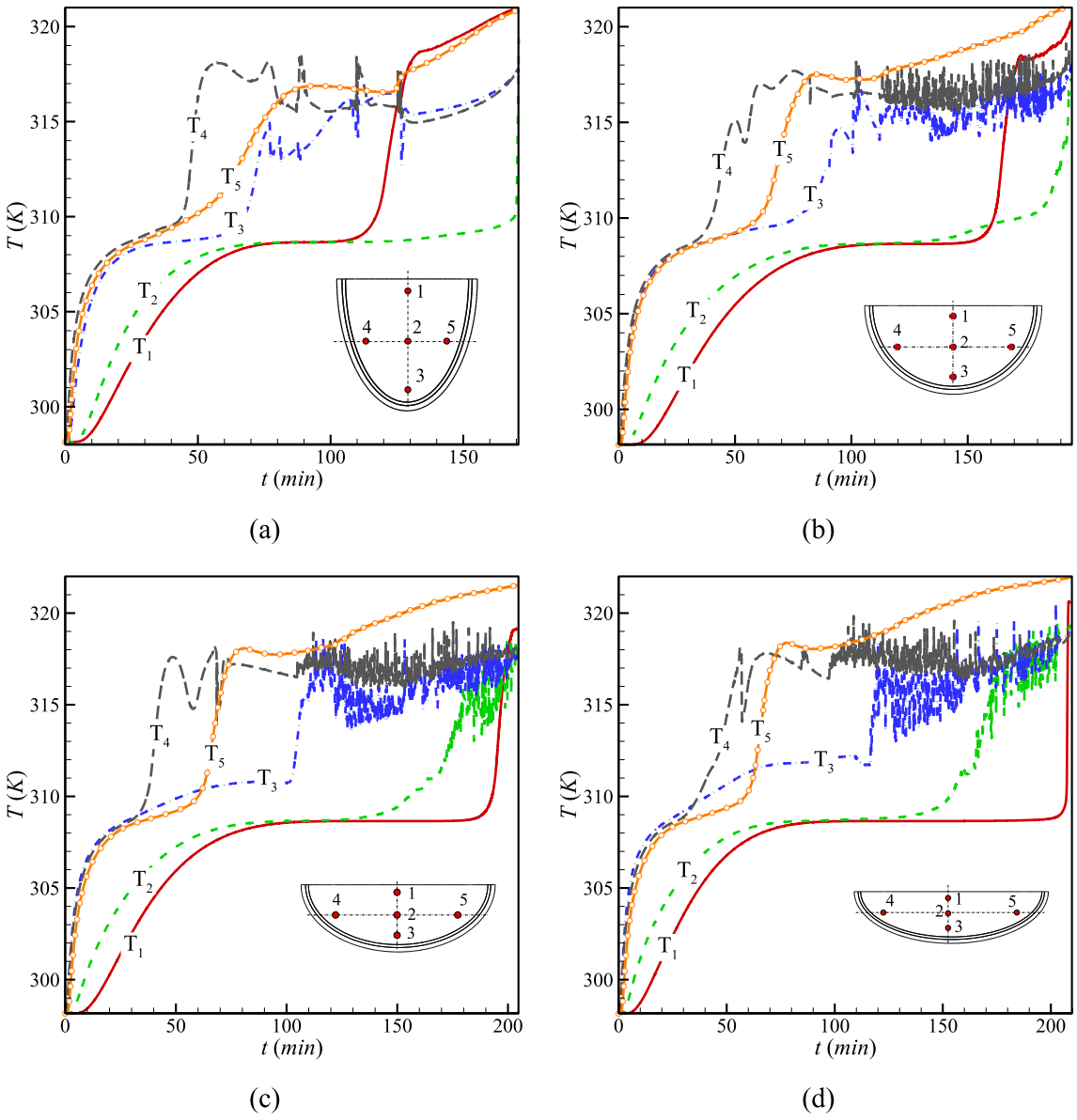

Fig. 10. Temperature histories of the different points of the LHTES unit during melting process for (a) $AR = 0.5$, (b) $AR = 1.0$, (c) $AR = 1.5$, and (d) $AR = 2.0$ at $\varphi =$ 0.5٪, and $\gamma = \pi/4$.

incompressible, and laminar. Taking into account these assumptions, the controlling equations of continuity, momentum, and energy for the HTS are [39,40]:

I) Continuity equation

$$\frac{\partial v_i}{\partial x_i} = 0 \tag{8}$$

II) Momentum equations

$$\rho_{HTF}\left[\frac{\partial v_i}{\partial t} + v_j\frac{\partial v_i}{\partial x_j}\right] = -\frac{\partial p}{\partial x_i} + \mu_{HTF}\frac{\partial^2 v_i}{\partial x_j \partial x_j} \tag{9}$$

III) Energy conservation

$$(\rho C_p)_{HTF}\frac{\partial T}{\partial t} + (\rho C_p)_{HTF} v_i\frac{\partial T}{\partial x_i} = \frac{\partial}{\partial x_i}\left(\lambda_{HTF}\frac{\partial T}{\partial x_i}\right) \tag{10}$$

3.3. Conduction heat transfer in the interface copper wall

Finally, the controlling equation of energy conservation for interface wall can be expressed as below [25,39]:

$$(\rho C_p)_{iw}\frac{\partial T}{\partial t} = \frac{\partial}{\partial x_i}\left(\lambda_{iw}\frac{\partial T}{\partial x_i}\right) \tag{11}$$

iw denotes the properties of the interface copper wall.

3.4. Boundary and initial conditions

The boundaries surrounding the NePCM domain are defined in mathematical forms as follows:

On the diameter of the semi-elliptical container as an adiabatic wall with no-slip and nonpermeability conditions [24]:

$$u = v = 0, \partial T \Big/ \partial y = 0 \; for \begin{cases} y = 0 \\ -a \le x \le a \end{cases} \tag{12a}$$

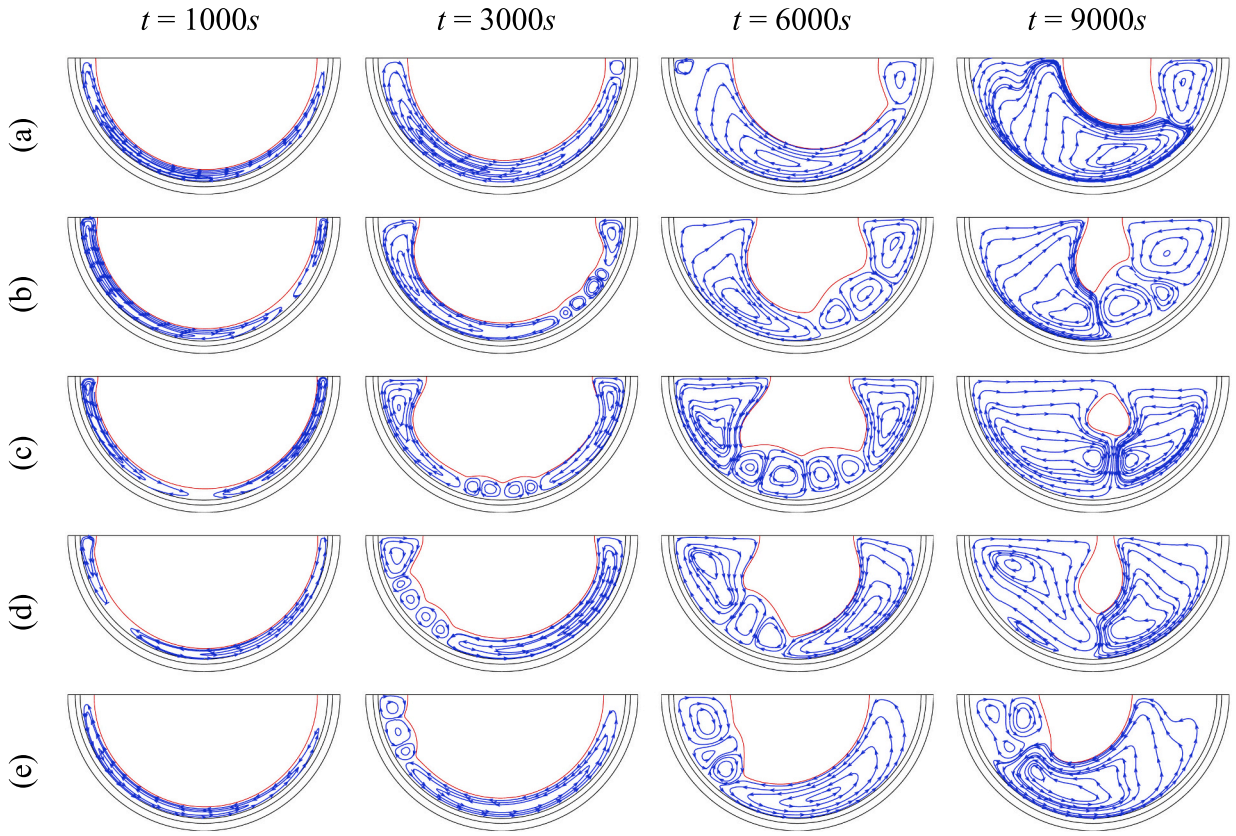

Fig. 11. Variations of Melted PCM domains and flow fields over time for (a): $\gamma = -\pi/2$, (b): $\gamma = -\pi/4$, (c): $\gamma = 0.0$, (d): $\gamma = \pi/4$, (e): $\gamma = \pi/2$ at $\varphi = 0.5\%$, and $AR = 1.0$.

On the interface of the copper wall and NePCM domain with no-slip and nonpermeability conditions [24]:

$$u = v = 0, (\lambda \partial T/\partial n)_{nepcm} = (\lambda \partial T/\partial n)_{iw} \; for \begin{cases} y \le 0 \\ \dfrac{x^2}{a^2} + \dfrac{y^2}{b^2} = 1 \end{cases} \tag{12b}$$

For the other surfaces of the copper wall, we have:

On the diameter of the semi-elliptical container as an adiabatic wall [24]:

$$(\lambda \partial T/\partial y)_{iw} = 0, for \begin{cases} y = 0 \\ -a - th_{iw} \le x \le -a \\ a \le x \le a + th_{iw} \end{cases} \tag{12c}$$

On the interface boundary of the copper wall and HTF channel [24]:

$$(\lambda \partial T/\partial n)_{HTF} = (\lambda \partial T/\partial n)_{iw} \; for \begin{cases} y \le 0 \\ \dfrac{x^2}{(a + th_{iw})^2} + \dfrac{y^2}{(b + th_{iw})^2} = 1 \end{cases} \tag{12d}$$

Finally, the following conditions are imposed on the bounds of the HTF channel:

On the outer boundary of the HTF channel as the adiabatic wall [24]:

$$(\lambda \partial T/\partial n)_{HTF} = 0 \; for \begin{cases} y \le 0 \\ \dfrac{x^2}{(a + th_{iw} + h_{HTF})^2} + \dfrac{y^2}{(b + th_{iw} + h_{HTF})^2} = 1 \end{cases} \tag{12e}$$

At the entrance of the channel:

$$u = 0.01 m \Big/ s, v = 0, and \; T = 323.15K \; for \begin{cases} y = 0 \\ -a - th_{iw} - h_{HTF} \le x \le -a - th_{iw} \end{cases} \tag{12f}$$

Initially, the whole domain is under the following state of temperature and velocity:

$$u = v = 0 \; and \; T = T_0 = 298.15K \tag{12g}$$

Before studying the melting process, it is necessary to define three important parameters. The total energy stored in the unit during melting flow is the summation of the sensible and latent heats, given by:

$$TES(t) = \underbrace{\int_{A_{nepcm}} \rho_{nepcm} C_{p,nepcm} (T - T_0)\, dA + \int_{A_{wall}} \rho_{wall} C_{p,wall} (T - T_0)\, dA}_{Sensible\ energy} + \underbrace{\int_{A_{nepcm}} \rho_{nepcm} L_{nepcm} dA}_{Latent\ energy} \tag{13}$$

the normalized melted liquid fraction can be calculated as:

$$MVF(t) = \frac{\int_A B(T) dA}{\int_A dA} \tag{14}$$

Finally, the power of the LHTES unit is:

$$POS = \frac{MVF|_{full\ melting\ time}}{full\ melting\ time} \tag{15}$$

4. Numerical method, grid independence test, and validation

4.1. Numerical method

In the current work, the enthalpy-porosity technique along with the adaptive mesh is applied for numerical modeling. As previously noted, this technique employs momentum source terms of $f_{m_i} = -(A_{mush}(1 - B(T))^2/B^3(T) + \varepsilon)v_i$ to suppress the velocity. The domain of NePCM can be

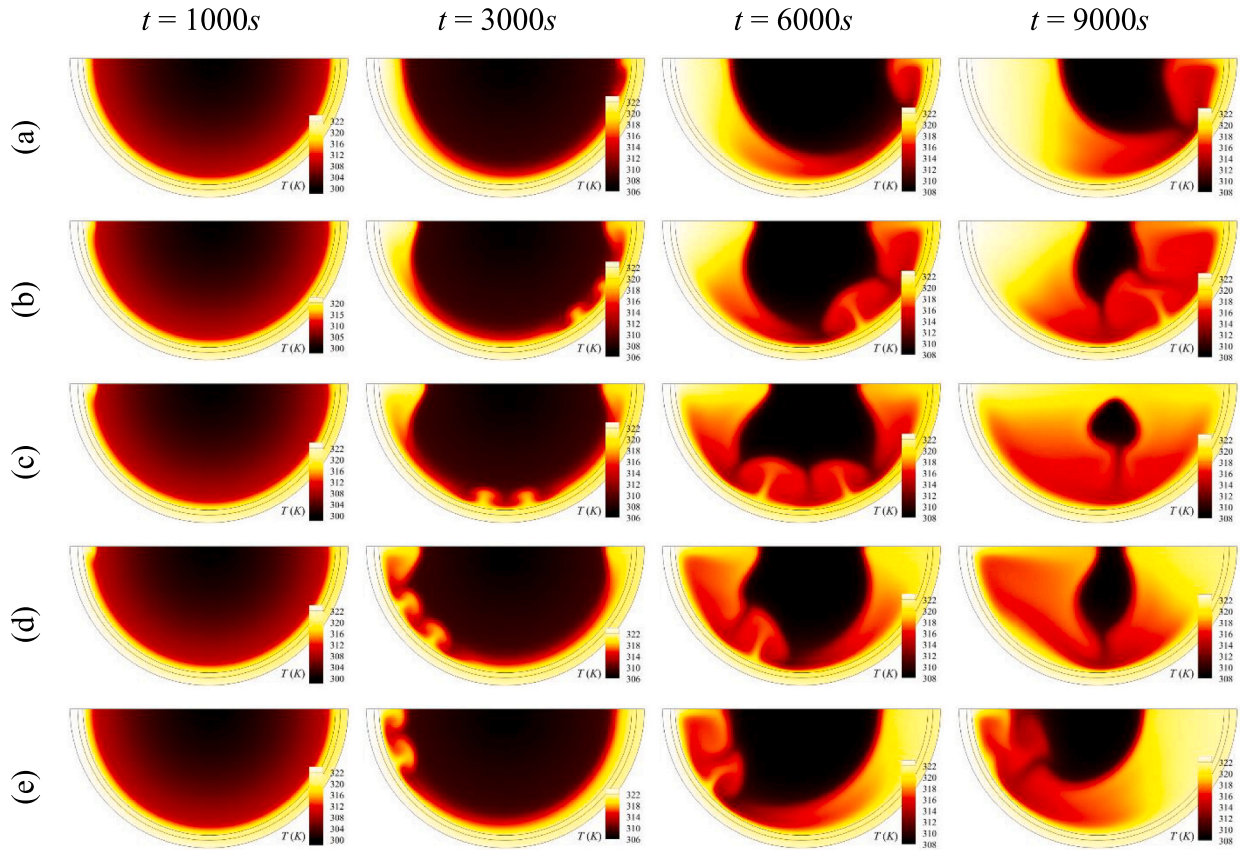

Fig. 12. Temperature fields over time for (a): $\gamma = -\pi/2$, (b): $\gamma = -\pi/4$, (c): $\gamma = 0.0$, (d): $\gamma = \pi/4$, (e): $\gamma = \pi/2$ at $\varphi = 0.5\%$, and $AR = 1.0$.

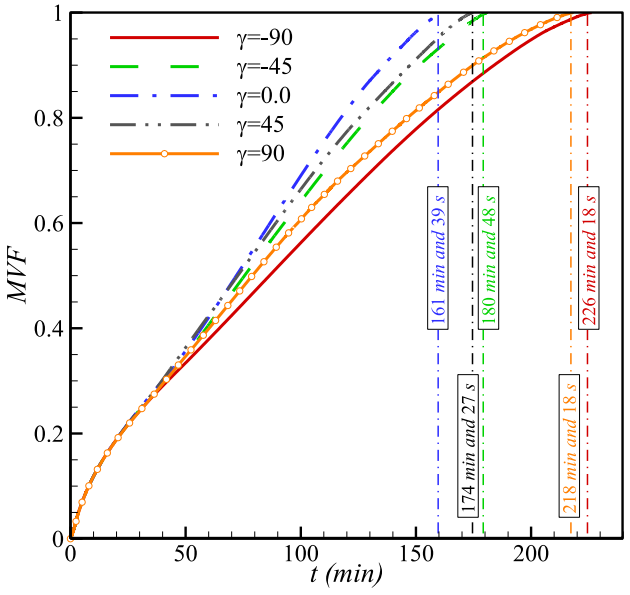

Fig. 13. Dependency of the *MVF* and the full melting time on the γ for $AR = 1$ and $\varphi = 1.0\%$.

divided into three subdomains of liquid, solid, and the area separating these two called the mushy zone. Considering the melting temperature, T_{me}, and melting temperature window, ΔT_{me}, these areas can be distinguished. The porous structure of the mushy zone comprising liquid and solid phases experiences a high-gradient velocity field. Also, the required energy to melt a unit volume of the NePCM, $-\rho_{snepcm} L_{nepcm} \partial B(T)/\partial t$, as a heat sink is added to the energy conservation equation. The mesh adoption technique is employed to fully consider all high-gradient parameters within the mushy zone, as this progressive method helps provide high-quality mesh. Solving the nonlinear differential equations mentioned before, the commercial code, COMSOL software, has been provided to implement the user-defined codes based on Galerkin finite element method [41,42]. For all of the variables (v_i, p, T) a first-order (straight-line) interpolation function between points has been used.

Specifying the bounded domain for the mesh adoption, a phase-field parameter, $pfp(T)$, is defined. In comparison to the melting temperature window, i.e. ΔT_{me}, the adaptive mesh refinement is applied at a larger gradient of the temperature, i.e. $3\Delta T_{me}/2$. Based on this wider temperature field, a thicker domain area of the melting interface is formed, leading to the smoother mesh transient along the interface zone. $pfp(T)$, the phase-field term is defined as:

$$pfp(T) = \begin{cases} 0 & T \le T_{me} - 3\Delta T_{me}/2 \\ 1 & T_{me} - 3\Delta T_{me}/2 < T < T_m + 3\Delta T_{me}/2 \\ 0 & T \ge T_{me} + 3\Delta T_{me}/2 \end{cases} \quad (25)$$

Also, there would be an adequate number of grid elements by considering the interface inside the grid adoption domain. This contributes to a less adoption process while employing a wider adoption zone across the interface.

Controlling the time step, a free step Backward Differentiation Formula (BDF) with a variable time step has been used. The maximum allowed time step is set to 0.2 s. The variable time step allows the solver to reduce the time step to ensure the stability of the code, especially at the beginning of the simulation. For the current study, the minimum time step adopted by the solver is in the range of 10^{-4} s. PARallel DIrect SOlver (PARDISO) solver with a Newtonian damping factor of 0.8 [43–45] has been employed to solve the residual equations, and subsequently, the iterations continue to satisfy the residual error of $O(10^{-6})$.

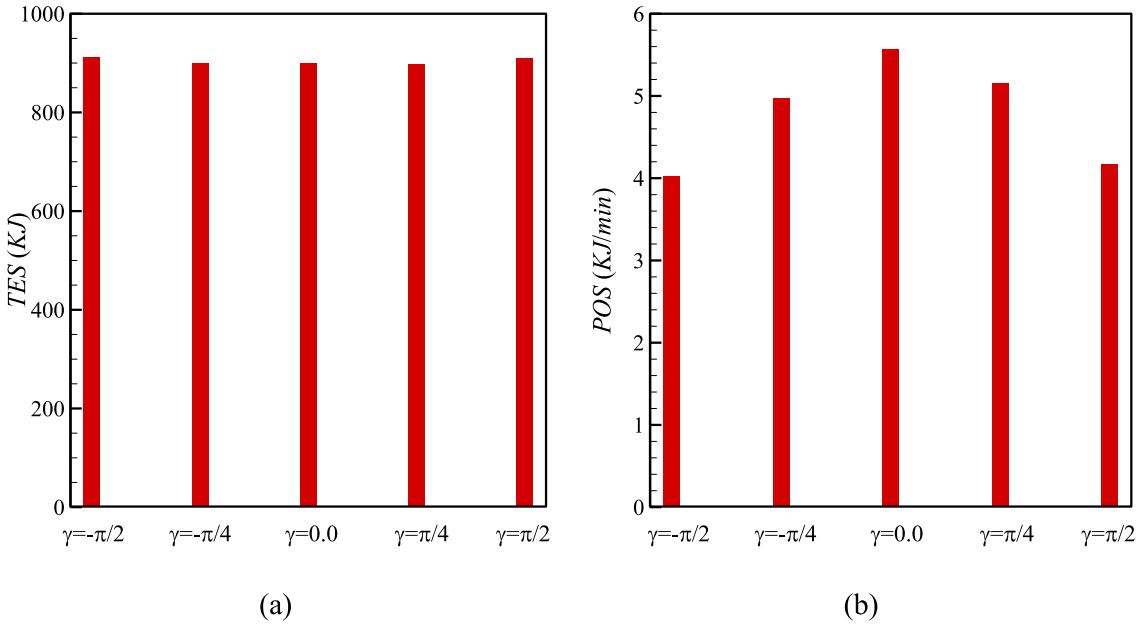

Fig. 14. Dependency of the *TES* and *POS* on the γ for $AR = 1.0$ and $\varphi = 1.0\%$.

4.2. Grid independence test

Achieving accurate results, the quality of grid should be checked. In this regard, four mesh cases of different element numbers are considered for grid independence test. It is worth noting that the triangular and rectangular elements are utilized to discretize the NePCM domain and the HTF channel, respectively. Two parameters of melt volume fraction (*MVF*) and local temperature (*T*) are chosen for the comparison of the results at $AR = 1.5$ for $\varphi = 0.5\%$, $\gamma = \pi/4$. As seen in Fig. 2(a), there is no difference between the variation of *MVF* in Grids 2 and 3. In addition, Fig. 2(b) depicts that the temperature history of Grids 3 and 4 is the same. So, grid case III including 7124 element numbers and computing time of 19 h, 56 min, and 23 s is utilized for numerical calculations due to decreasing the time and cost of simulations (See Table 3). The adaptive mesh provided at four different time steps of $t = 1000$s, $t = 3000$ s, $t = 6000$ s, and $t = 9000$ s is demonstrated when $AR = 1.5$, $\varphi = 0.5\%$, $\gamma = \pi/4$ in Fig. 3. A smooth grid transition is evident based on this figure.

4.3. Validation

In order to verify the accuracy and correctness of the results, validation of the results by former researches is a vital step. The research of Kamkari et al. [46] is the first case of validation. They numerically and experimentally investigated the melting of the PCM inside a rectangular cavity. Fig. 4 demonstrates the experimental and numerical results of Ref. [46] against the results of the present research. The melting process at different time steps after 10 min, 20 min, 30 min, and 40 min of the start of simulations is shown in this figure for $Ra = 8.3 \times 10^8$. As seen, there is a good agreement between the numerical results of the current study and those of Ref. [46]. Another case of validation refers to the investigation of Xu et al. [47]. The temperature of a certain point inside the cavity at different time steps is chosen as the validation parameter. The boundary conditions of the cavity include the horizontal adiabatic walls and high- and low-temperature vertical walls. According to Fig. 5, a desirable agreement is evident between the results of the present study and Ref [47].

5. Results and discussion

This study investigates the dependency of the *MVF*, the total energy stored, and the governing fields in the LHTES semi-elliptical unit on the aspect ratio ($0.5 \leq AR \leq 2$), the concentration of the nano additives ($0.0 \leq \varphi \leq 0.03$), and the inclination angle of the unit ($-\pi/2 \leq \gamma \leq \pi/2$).

5.1. Study of effects of aspect ratio (AR)

Figs. 6 and 7 demonstrate the melted PCM domains, streamlines, and temperature fields of the PCM in the domain study for different *AR* values at $\gamma = \pi/4$ and $\varphi = 0.5\%$. As seen in Fig. 6, at the primary time step of the melting process ($t = 1000$ s), the area where the melted PCM moves is tight. The friction losses are dominant at this time step, so there is a weak fluid flow. At $t = 3000$ s, these initial movements are enhanced and a regular pattern of cells are formed in the direction of the flow known as "Benard cells". At $t = 6000$ s, these cells are getting larger and joining to each other, leading to occupy more space of PCM area. The zone of liquid PCM is getting larger as time passes. It should be noted that the amount of PCM is equal for all *AR* ranges. At $t = 9000$ s, most of PCMs are melted, and among the *AR* cases, $AR = 0.5$ indicates the highest amount of melted PCM. The PCM of this time sequence and configuration remains at the center of the semi-elliptical domain which shows a different pattern by the other configurations. Furthermore, at this geometrical design, the melting area covers all around the solid core of PCM while for other cases ($AR = 1.0$, 1.5, 2.0) it moves from the bottom to up side of the semi-elliptical.

As seen in Fig. 7, at $t = 1000$s, the conduction heat transfer mechanism plays the main role in this area, and there is no significant convective. The threshold of melting is 310 K, therefore, the areas warmer than this temperature experience the melting, and the cooler ones keep solid. As time passes, the free convection increases due to the density difference, and the front of melted area develops to the center of the semi-elliptical container. At $t = 9000$ s, finally, most of the PCM is melted except a small zone at the center of the domain. It can be seen that the molten area is larger for lower *AR* values. This is due to the exerted buoyancy forces are higher in the lower *AR*.

Fig. 8 shows the *MVF* and time required for melting the whole PCM for different values of *AR* at $\gamma = \pi/4$ and $\varphi = 0.5\%$. The *MVF* rate looks identical for all configurations at initial times ($t < 50$ min). Furthermore,

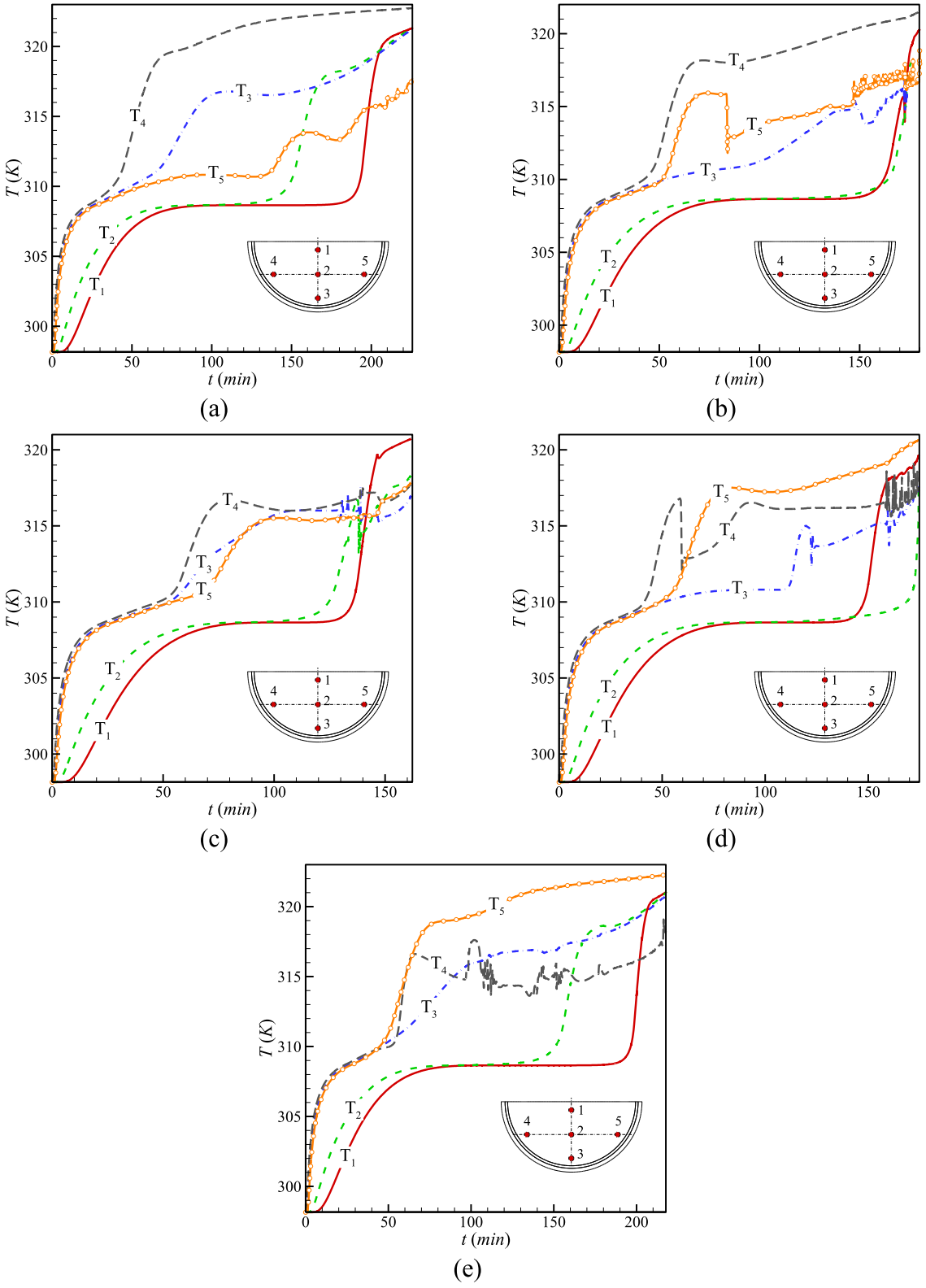

Fig. 15. Temperature histories of the different points of the LHTES unit during melting recess for (a) $\gamma = -\pi/2$, (b) $\gamma = -\pi/4$, (c) $\gamma = 0.0$, and (d) $\gamma = \pi/4$, and (e) $\gamma = \pi/2$ at $AR = 1$, and $\varphi = 1.0\%$.

the *MVF* appears to be the same for all *AR* values at $t < 150$ min, except $AR = 0.5$. It is seen that the domain design of $AR = 0.5$ contributes to the lowest time of melting, around $t = 170$ min while the longest time of melting devotes to the design of $AR = 2$, around $t = 208$ min. The full melting time of $AR = 0.5$ is decreased about 12% compared to that of $AR = 1.0$. In fact, stronger buoyancy forces at lower *AR* values reduce the full melting time.

It is worth noting that the latent stored energy is equal for all

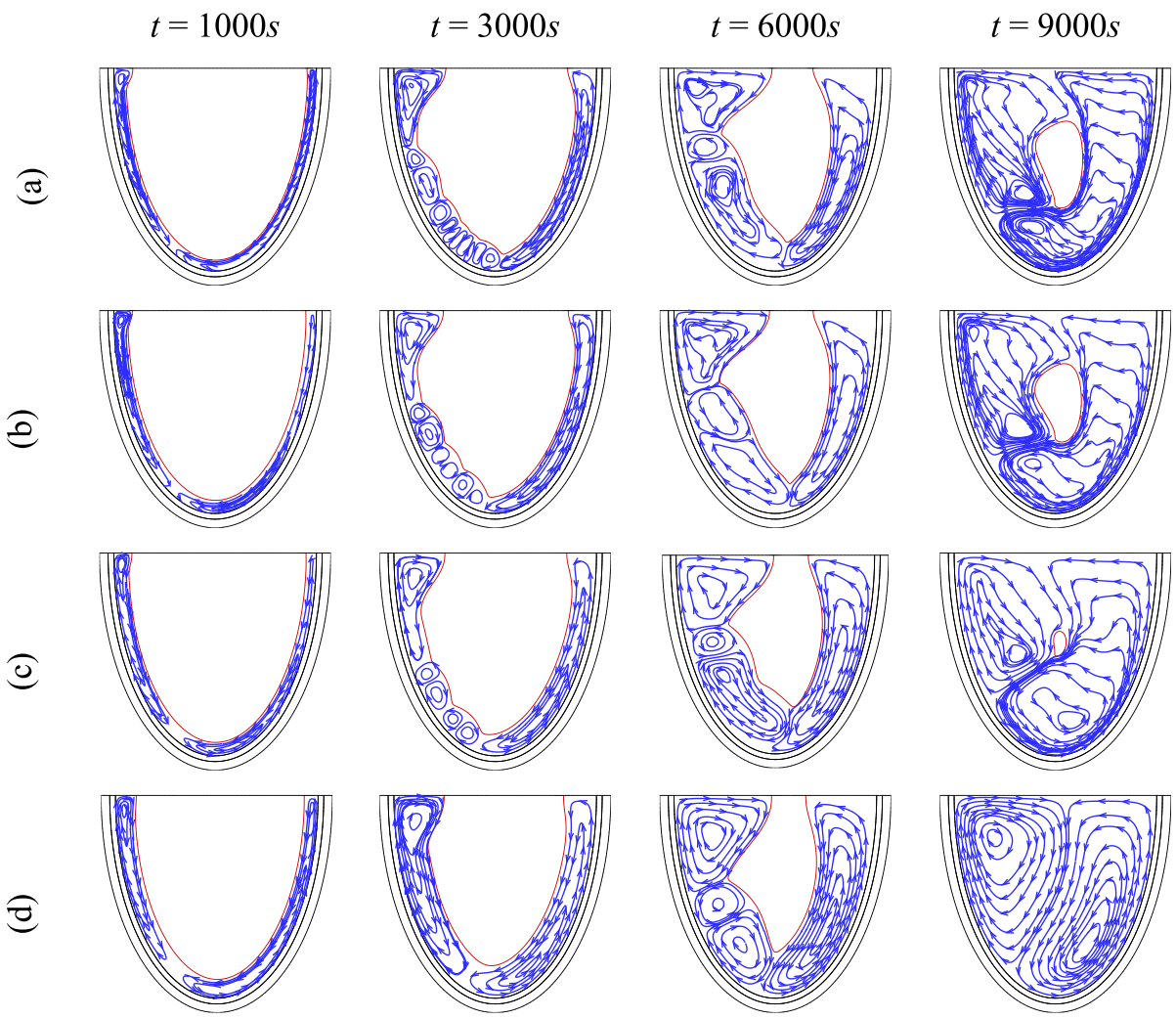

Fig. 16. Melted PCM domains and flow fields over time for (a): $\varphi = 0.0\%$, (b): $\varphi = 0.5\%$, (c): $\varphi = 1.0\%$, (d): $\varphi = 3.0\%$ at $\gamma = \pi/4$, and $AR = 0.5$.

configurations of the LHTES unit because as mentioned before the amount of PCM is the same for all structures. Also, there is no significant difference in the stored sensible energy of the units. For example, the sensible energy is the same for the aspect ratios of $AR = 1$ and $AR = 1.5$. The increase of the total energy for the units of $AR = 0.5$ and $AR = 2.0$ compared to $AR = 1$ is 0.21% and 65%, respectively (Fig. 9(a)). As shown in Fig. 9(b), the power of energy storage unit is maximum for $AR = 0.5$. The power of system for aspect ratio of $AR = 0.5$ is higher than the aspect ratio of $AR = 1.0$, around 13.9%. Furthermore, this reducing range for the aspect ratio of $AR = 1.5$ and $AR = 2.0$ compared to $AR = 1.0$ are 4.8% and 6.4%, respectively.

Considering the temperature history for specified points inside the domain study, more complete data around the characteristic of the melting of PCM inside the enclosure can be achieved. Fig. 10 illustrates the effect of different values of the AR on the temperature histories of the different points of the LHTES unit at $\varphi = 0.5\%$, and $\gamma = \pi/4$. The coordinates of the defined points are $(0, -b/8)$, $(0, -b/2)$, $(0, -b/1.2)$, $(-a/1.5, -b/2)$, and $(a/1.5, -b/2)$ for the points 1, 2, 3, 4, and 5, respectively. As previously mentioned in the mathematical model section, a, and b are the radii of the semi-elliptical container in the in x and y directions.

At the primary times ($t < 30$ min), as there is no melting of PCM and no convective effects, points of 3, 4 and, 5 almost show the same temperature raised by the conductive mechanism. This upward trend of temperature continues up to the start of melting. Generally, a sharp increase in temperature is evident at points where the melt front is reaching them. Afterward, the temperature fluctuates or increases moderately up to the terminating of the melting process.

The temperature fluctuations demonstrate the transient vortices formed in the melted NePCM flow. Furthermore, mitigation of these fluctuations shows that these temporal fluctuations join to each other to form larger vortices. Also, it can be said that the observed temperature fluctuations increase by the aspect ratio growth, which approves the strong existence of temporal chaotic vortices in the melted NePCM flow. As seen in the temperature history diagram, point 2 does not experience any fluctuation during the melting process in the aspect ratios of $AR = 0.5$ and $AR = 1$. Because the melt front reaches these points at the end of the melting process of the whole enclosure for these aspect ratios.

5.2. *Effects of inclination angle (γ)*

Figs. 11 and 12 depict the effect of various inclination angles on the melted PCM domains, streamlines and, temperature fields of the NePCM at different time instants for $\varphi = 0.5\%$ and $AR = 1.0$. At primary time snap ($t = 1000$s), conduction is the predominant mechanism. This model of heat transfer lasts while the viscous force is more powerful against the fluid motion. Whilst melting enhances ($t = 3000$ s), vorticities are formed. In the cases of $\gamma = -\pi/2$ and $\gamma = -\pi/4$, the large and weak vorticities are formed at the area close to the HTF entrance and top of the semi-elliptical, while the small vortices are seen at the lower part. On the

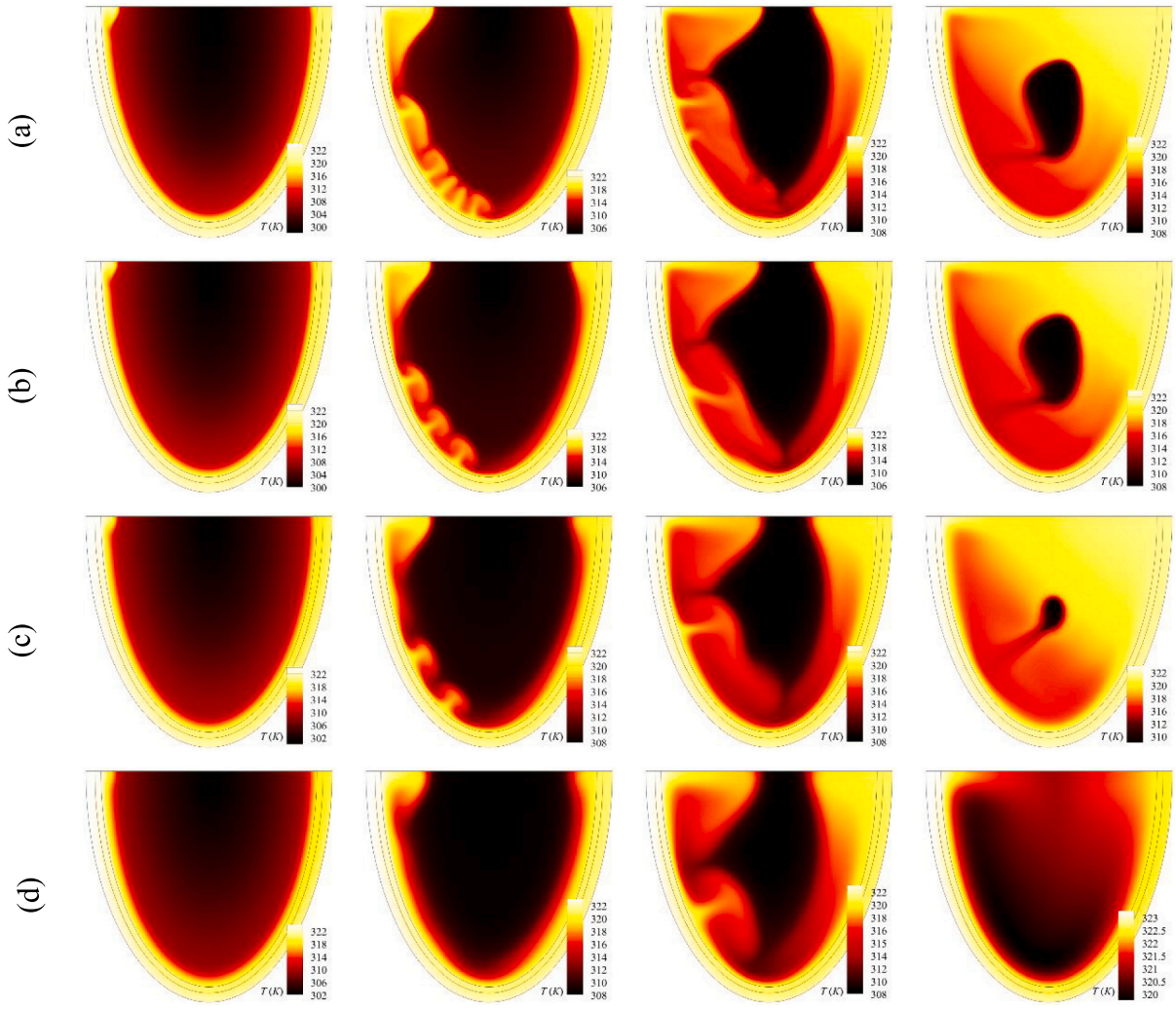

Fig. 17. Melted PCM domains and temperature fields over time for (a): $\varphi = 0.0\%$, (b): $\varphi = 0.5\%$, (c): $\varphi = 1.0\%$, (d): $\varphi = 3.0\%$ at $\gamma = \pi/4$, and $AR = 0.5$.

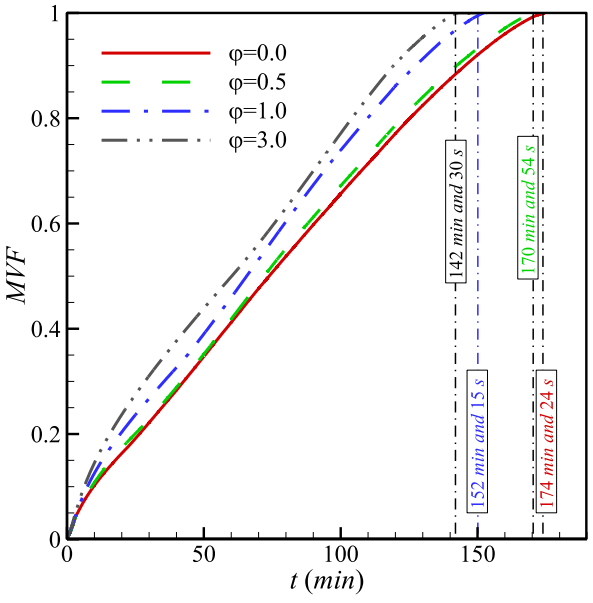

Fig. 18. Dependency of the *MVF* and the full melting time on the φ for $AR = 0.5$ and $\gamma = \pi/4$.

other hand, at the case of $\gamma = \pi/2$ and $\gamma = \pi/4$, the small and strong vorticities are formed at the zones near the entrance of the HTF. For $\gamma = 0$, transient small vorticities are created at the middle of the semi-elliptical and bigger ones out of this area toward the entrance and end of the domain. This trend continues for $t = 6000$ s and the fluid PCM prevails. At final time step ($t = 9000$ s), $\gamma = 0$ displays the highest rate of molten PCM. This is due to equal effects of left and right sides fluid vortices contributing to a uniform melting inside the semi-circle. Also, it can be seen in the temperature field that finally, the most portion of the liquid PCM is accumulated at the left side and right side of the domains for $\gamma = -\pi/2$ and $\gamma = \pi/2$, respectively.

Fig. 13 shows the *MVF* and the time taking for complete melting of the NePCM in different inclinations of the domain at $AR = 1$ and $\varphi = 1.0$. At the primary time, $t < 40$ min, all configurations indicate the same rate of melting due to the dominant conductive pattern. As seen, the configuration of $\gamma = 0$ needs the lowest time for quit melting of PCM (~ 161 mins) because of the uniform melting pattern. The inclination of $\gamma = -\pi/2$ shows the longest time of melting (~226 mins). This is due to the lower effects of the convective mechanism while the hotter part of NePCM is at the upper part of the semi-circle. Both designs of $\gamma = -\pi/4$ and $\gamma = \pi/4$ have the approximately same time of melting.

According to Fig. 14(a), the stored sensible energy depends slightly on the rotation angle (γ) of the LHTES unit. In this regard, the maximum deviation from the total stored energy in the horizontal unit is appointed to the system of $\gamma = -\pi/4$, which is −1.3%. Thus, based on the time of

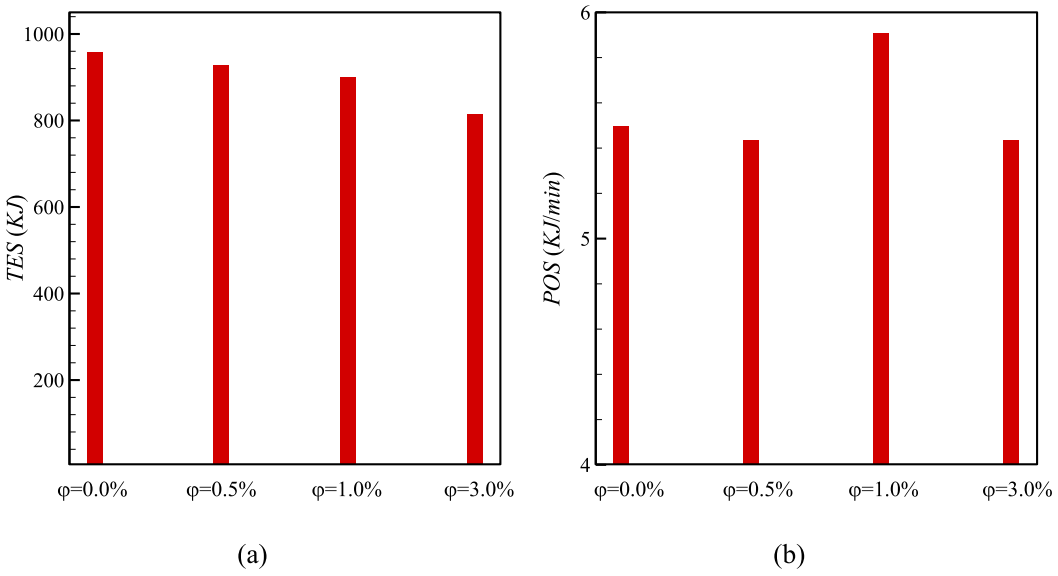

Fig. 19. Dependency of the *TES* and *POS* on the φ for $AR = 0.5$ and $\gamma = \pi/4$.

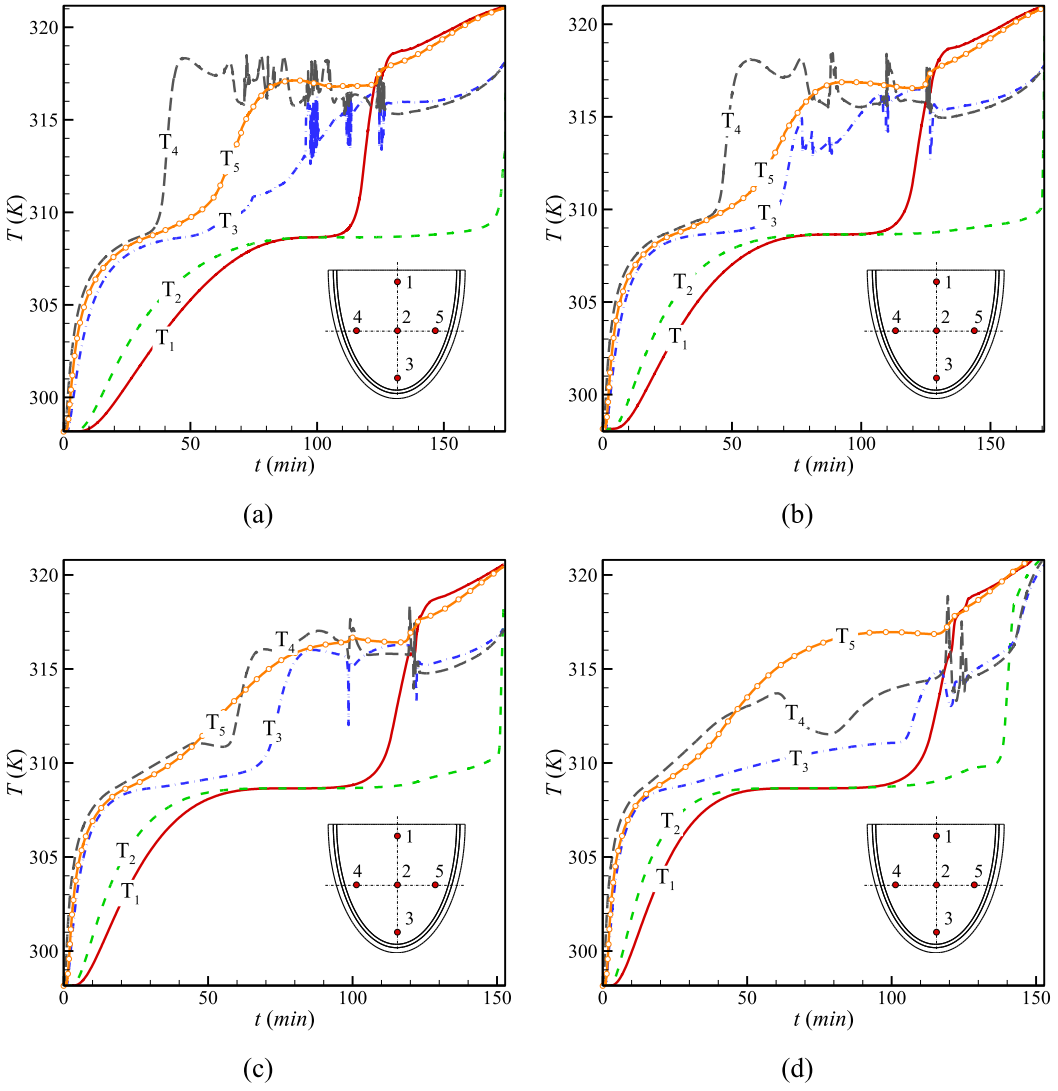

Fig. 20. Temperature histories of the different points of the LHTES unit during melting process for (a) $\varphi = 0.0\%$, (b) $\varphi = 0.5\%$, (c) $\varphi = 1.0\%$, and (d) $\varphi = 3.0\%$ at $AR = 0.5$, and $\gamma = \pi/4$.

full melting mentioned above, it can be admitted that the system has the highest power in the horizontal configuration (Fig. 14(b)).

Fig. 15 shows the temperature history of different points within the domain for different inclination values of the LHTES unit at $\varphi = 1.0\%$, and $AR = 1.0$. At primary time steps ($t < 50$ mins), the temperature trend of points near to the HTF (T_4, T_3 and, T_5) are roughly identical because these locations are under the conductive mechanism. The diversity of final temperature between T_4 and T_5 for the cases of (a) and (e) can be explained by the convective mechanism which the melted hot NePCM moves to the upper part of the semi-circle.

For $\gamma = -\pi/2$, point 4 locates at the highest part and experiences melting sooner than the other points. So, the highest temperature devotes to this point. Considering the temperature fields of the former figure, it is seen that the conductive is the predominant mechanism during the melting process, so there are no temporal powerful vortices contributing to the temperature fluctuation. For $\gamma = -\pi/4$, the temperature of point 5 reduces intrusively at $t = 85$ mins. Actually, the formation and growth of the vortices (according to temperature field) is done nearby point 5 at this angle. And the intense fall of temperature at point 5 is the result of the accumulation of powerful temporal vortices to create consistent vortices. For $\gamma = 0$ (Fig. 15 (c)), as depicted in the above figures of temperature fields, temperature flames are made and grown at the most bottom part, i.e. point 3. Trying to unite these temperature flames leads to temperature fluctuations at point 3. This trend is the reason for intense temperature fluctuations at point 2, too.

5.3. Effects of the presence of nano-additives (φ)

Figs. 16 and 17 demonstrate the effect of various concentrations of the nano-additives on the melted NePCM domain, streamlines, and temperature field of the LHTES units at $\gamma = \pi/4$, and $AR = 0.5$. At $t =$ 1000s, there is not a significant difference in the melted NePCM domains and temperature field diagrams among all the cases. At $t = 3000$ s, small vortices are formed for lower concentration ranges and larger ones are created in the concentration value of $\varphi = 3.0\%$. Actually, the number of Benard cells reduces at this time sequence, as all cells join to each other at a mass fraction of 3.0% and make a united cell. This refers to the rise of viscosity of NePCM due to the increase in the nano-additives mass fraction.

As time passes, liquid NePCM takes more space of the domain, and this trend is more apparent for the higher concentrations of the nanoparticles. Generally, two thermophysical parameters of viscosity and thermal conductivity can affect the melting domain, significantly. Adding the nano-additives to the PCM augments these parameters. Increasing thermal conductivity and viscosity are desirable and non-desirable parameters, respectively. Results indicate that the desired effect of thermal conductivity enhancement can dominate the undesirable impacts of viscosity. It can be seen that at the final time snaps most of the domain is covered by the melted NePCM, especially for the case of $\varphi =$ 3.0% contributing to overall melting. Also, as seen in Fig. 17(d), the taken heat from HTF after complete melting increases the temperature of the melted NePCM significantly at $t = 9000$ s.

Fig. 18 shows the time of full melting for different concentrations of nano-additives. It is seen that a higher concentration of the nano-additives leads to a lower full melting time. It is worth mentioning that the concentration value of $\varphi = 0.5\%$ does not affect the melting time, considerably. Adding the nano-additives to the pure PCM increases thermal conductivity, leading to a reduction in melting time. Moreover, a decrease in the latent heat due to the presence of the nanoparticles can reduce the melting time, as a lower amount of energy is needed for complete melting process. The total stored energy reduces by the increase in nano-additives mass fraction based on Fig. 19(a). Its main reason is the reduction in the specific latent heat of NePCM during melting due to the existence of nano-additives (see Table 2). Fig. 19(b) demonstrates the power of the energy storage system, the ratio of the total energy stored to the melting time, for various mass fractions. Results show that although the time of melting reduces considerably for the mass fraction of 3%, the power of system reduces due to the decrease in stored energy. It is worth mentioning that the unit power is equal for 0.5% and 3.0% mass fraction. By increasing the mass fraction of nanoparticles, both numerator and denominator terms in the definition of the power of system decreases (see Eq. (15)). For nanoparticles with mass fractions of 0.5% and 3%, the amount of reduction in the numerator is higher than the reduction in the denominator, and hence the overall power decreases. Additionally, the unit of nano-additives mass fraction of $\varphi = 1.0\%$ has the highest energy storage capacity, about 7.2% more than that of pure PCM. Indeed, for the unit of $\varphi = 1.0\%$, the amount of reduction in the stored energy due to adding the nano-additives is lower than the reduction in the melting time, consequently, the power of the system increases.

Fig. 20 illustrates the temperature history of points inside the semi-elliptical container for different concentrations of the nano-additives. It is seen that the temperature fluctuations reduce by the increase of nano-additives mass fraction. This is because the strength of the melted liquid flow declines with an increase in the nano-additives fraction. There are no temperature fluctuations at point 3 when the mass fraction of nano-additives is 3.0%. This is due to the stronger vortices based on increased viscosity of distributed higher nano-additives ranges.

6. Conclusion

In this study, the transient phase change flow of an energy storage system in a semi-elliptical domain has been investigated. This system contains a channel of heat transfer fluid (HTF), that the thermal energy transfers from this fluid to the PCM by a coppery interface wall. The semi-elliptical system of different aspect ratios has the inclination angle γ to the horizontal line, and the PCM is boosted by the nanoparticles. The PCM volume occupying the enclosure is considered to be a constraint. The enthalpy-porosity method with a constant grid using the mesh-adoption technique is employed to simulate this transient process. The numerical results indicate that the total time of melting and consequently the power of system increase by reduction of AR. Additionally, the temperature fluctuations decrease by the AR reduction. Also, it is observed that the full time of melting and the power of system experience their maximum at the horizontal configuration. Ultimately, adding nanoparticles reduces the melting time and the stored energy, significantly. Compared to the systems filled with pure PCM, the cases of nano mass fraction values of $\varphi = 0.5\%$ and $\varphi = 3\%$ demonstrate a reduction in the unit power. Nevertheless, the system of nano-PCM value of $\varphi = 1\%$ shows the maximum power compared to other cases.

As a possible future study, the effect of the metal foam on the thermal performance of the semi-elliptical LHTES system can be focused on. Also, different structures of the system with horizontal, vertical, or radial fins can be investigated to identify their impacts on the unit's thermal performance. Moreover, the thermal performance of the system (i.e. melting time, unit capacity, etc.) in a cycle including the melting and solidifications process can be explored.

Declaration of Competing Interest

The authors declare that they have no conflict of interest.

Acknowledgments

The authors extend their appreciation to the Deanship of Scientific Research at King Khalid University, Abha, Saudi Arabia for funding this work through the Research Group under grant number (R.G.P.1/329/42).

References

[1] J.M. Mahdi, S. Lohrasbi, D.D. Ganji, E.C. Nsofor, Accelerated melting of PCM in energy storage systems via novel configuration of fins in the triplex-tube heat exchanger, Int. J. Heat Mass Transf. 124 (2018) 663–676.

[2] P.K.S. Rathore, S.K. Shukla, Enhanced thermophysical properties of organic PCM through shape stabilization for thermal energy storage in buildings: a state of the art review, Energy Build. (2021) 110799.

[3] R. Saxena, D. Rakshit, S. Kaushik, Review on PCM application for cooling load reduction in Indian buildings, in: Solar Energy, Springer, 2020, pp. 247–275.

[4] F. Javadi, H. Metselaar, P. Ganesan, Performance improvement of solar thermal systems integrated with phase change materials (PCM), a review, Sol. Energy 206 (2020) 330–352.

[5] M. Elashmawy, M. Alhadri, M.M. Ahmed, Enhancing tubular solar still performance using novel PCM-tubes, Desalination 500 (2021), 114880.

[6] G.S. Wahile, P.D. Malwe, A.V. Kolhe, Waste heat recovery from exhaust gas of an engine by using a phase change material, Mat. Today Proc. 28 (2020) 2101–2107.

[7] Q. Al-Yasiri, M. Szabó, Influential aspects on melting and solidification of PCM energy storage containers in building envelope applications, Int. J. Green Energy (2021) 1–21.

[8] S.R.L. da Cunha, J.L.B. de Aguiar, Phase change materials and energy efficiency of buildings: a review of knowledge, J. Energy Storage 27 (2020), 101083.

[9] S. Nižetić, M. Jurčević, M. Arıcı, A.V. Arasu, G. Xie, Nano-enhanced phase change materials and fluids in energy applications: a review, Renew. Sust. Energ. Rev. 129 (2020), 109931.

[10] S.L. Tariq, H.M. Ali, M.A. Akram, M.M. Janjua, M. Ahmadlouydarab, Nanoparticles enhanced phase change materials (NePCMs)-A recent review, Appl. Therm. Eng. (2020) 115305.

[11] L.-L. Tian, X. Liu, S. Chen, Z.-G. Shen, Effect of fin material on PCM melting in a rectangular enclosure, Appl. Therm. Eng. 167 (2020), 114764.

[12] C.R. Raj, S. Suresh, R. Bhavsar, V.K. Singh, K.A. Govind, Influence of fin configurations in the heat transfer effectiveness of solid solid PCM based thermal control module for satellite avionics: numerical simulations, J. Energy Storage 29 (2020), 101332.

[13] A. Arshad, M. Jabbal, P.T. Sardari, M.A. Bashir, H. Faraji, Y. Yan, Transient simulation of finned heat sinks embedded with PCM for electronics cooling, Therm. Sci. Eng. Progr. 18 (2020), 100520.

[14] N.S. Bondareva, M.A. Sheremet, Effect of the time-dependent volumetric heat flux on heat transfer performance inside a heat sink based on the phase change materials, Clean Techn. Environ. Policy (2020) 1–10.

[15] P.T. Sardari, R. Babaei-Mahani, D. Giddings, S. Yasseri, M. Moghimi, H. Bahai, Energy recovery from domestic radiators using a compact composite metal foam/PCM latent heat storage, J. Clean. Prod. 257 (2020), 120504.

[16] P. Talebizadehsardari, et al., Effect of airflow channel arrangement on the discharge of a composite metal foam-phase change material heat exchanger, Int. J. Energy Res. 45 (2020) 2593–2609.

[17] J.M. Mahdi, H.I. Mohammed, E.T. Hashim, P. Talebizadehsardari, E.C. Nsofor, Solidification enhancement with multiple PCMs, cascaded metal foam and nanoparticles in the shell-and-tube energy storage system, Appl. Energy 257 (2020), 113993.

[18] P.T. Sardari, H.I. Mohammed, D. Giddings, M. Gillott, D. Grant, Numerical study of a multiple-segment metal foam-PCM latent heat storage unit: effect of porosity, pore density and location of heat source, Energy 189 (2019), 116108.

[19] Y. Tao, Y.-L. He, A review of phase change material and performance enhancement method for latent heat storage system, Renew. Sust. Energ. Rev. 93 (2018) 245–259.

[20] B.E. Jebasingh, A.V. Arasu, A comprehensive review on latent heat and thermal conductivity of nanoparticle dispersed phase change material for low-temperature applications, Energy Storage Mat. 24 (2020) 52–74.

[21] N.S. Bondareva, B. Buonomo, O. Manca, M.A. Sheremet, Heat transfer inside cooling system based on phase change material with alumina nanoparticles, Appl. Therm. Eng. 144 (2018) 972–981.

[22] X. Ma, M. Sheikholeslami, M. Jafaryar, A. Shafee, T. Nguyen-Thoi, Z. Li, Solidification inside a clean energy storage unit utilizing phase change material with copper oxide nanoparticles, J. Clean. Prod. 245 (2020), 118888.

[23] F. Li, M. Jafaryar, M.R. Hajizadeh, Q.-V. Bach, Performance of ventilation system involving thermal storage unit considering porous media, J. Energy Storage 31 (2020), 101709.

[24] H. Faraji, M. El Alami, A. Arshad, Investigating the effect of single and hybrid nanoparticles on melting of phase change material in a rectangular enclosure with finite heat source, Int. J. Energy Res. 45 (3) (2021) 4314–4330.

[25] N.S. Bondareva, B. Buonomo, O. Manca, M.A. Sheremet, Heat transfer performance of the finned nano-enhanced phase change material system under the inclination influence, Int. J. Heat Mass Transf. 135 (2019) 1063–1072.

[26] N.S. Bondareva, M.A. Sheremet, Effect of nano-sized heat transfer enhancers on PCM-based heat sink performance at various heat loads, Nanomaterials 10 (1) (2020) 17.

[27] Y.-M. Chu, D. Yadav, A. Shafee, Z. Li, Q.-V. Bach, Influence of wavy enclosure and nanoparticles on heat release rate of PCM considering numerical study, J. Mol. Liq. 319 (2020), 114121.

[28] M. Sheikholeslami, R.-U. Haq, A. Shafee, Z. Li, Heat transfer behavior of nanoparticle enhanced PCM solidification through an enclosure with V shaped fins, Int. J. Heat Mass Transf. 130 (2019) 1322–1342.

[29] A.B. Albadarin, T.K. Ibrahim, M.M. Selim, A. Issakhov, Z. Li, Simulation of sinusoidal enclosure filled with nanoparticles enhanced PCM, J. Mol. Liq. 337 (2021) 116388.

[30] M. Bechiri, K. Mansouri, Analytical study of heat generation effects on melting and solidification of nano-enhanced PCM inside a horizontal cylindrical enclosure, Appl. Therm. Eng. 104 (2016) 779–790.

[31] S.A.M. Mehryan, M. Ghalambaz, L. Sasani Gargari, A. Hajjar, M. Sheremet, Natural convection flow of a suspension containing nano-encapsulated phase change particles in an eccentric annulus, J. Energy Storage 28 (2020) 101236, https://doi.org/10.1016/j.est.2020.101236, 04/01/2020.

[32] D. Groulx, P.H. Biwole, M. Bhouri, Phase change heat transfer in a rectangular enclosure as a function of inclination and fin placement, Int. J. Therm. Sci. 151 (2020), 106260.

[33] B. Kamkari, H. Shokouhmand, F. Bruno, Experimental investigation of the effect of inclination angle on convection-driven melting of phase change material in a rectangular enclosure, Int. J. Heat Mass Transf. 72 (2014) 186–200.

[34] P.H. Biwole, D. Groulx, F. Souayfane, T. Chiu, Influence of fin size and distribution on solid-liquid phase change in a rectangular enclosure, Int. J. Therm. Sci. 124 (2018) 433–446.

[35] M. Bechiri, K. Mansouri, S. Saleem, Study of heat sink effects during melting of constrained phase change material inside a spherical enclosure, J. Energy Storage 27 (2020), 101151.

[36] Z.-Q. Zhu, et al., Inward solidification heat transfer of nano-enhanced phase change materials in a spherical capsule: an experimental study, J. Heat Transf. 140 (2) (2018).

[37] M. Al-Jethelah, S. Ebadi, K. Venkateshwar, S.H. Tasnim, S. Mahmud, A. Dutta, Charging nanoparticle enhanced bio-based PCM in open cell metallic foams: an experimental investigation, Appl. Therm. Eng. 148 (2019) 1029–1042, https://doi.org/10.1016/j.applthermaleng.2018.11.121, 02/05/2019.

[38] S.-K. Choi, S.-O. Kim, T.-H. Lee, Dohee-Hahn, Computation of the natural convection of nanofluid in a square cavity with homogeneous and nonhomogeneous models, Numer. Heat Transf. Part A: Appl. 65 (4) (2014) 287–301.

[39] M. Sen, Lecture Notes on Intermediate Fluid Mechanics, 1996.

[40] X. Wen, L.-P. Wang, Z. Guo, J. Shen, An improved discrete unified gas kinetic scheme for simulating compressible natural convection flows, J. Comp. Phys. X 11 (2021), 100088.

[41] J.N. Reddy, D.K. Gartling, The Finite Element Method in Heat Transfer and Fluid Dynamics, CRC Press, 2010.

[42] O.C. Zienkiewicz, R.L. Taylor, P. Nithiarasu, The Finite Element Method for Fluid Dynamics, Elsevier, 2015.

[43] O. Schenk, K. Gärtner, Solving unsymmetric sparse systems of linear equations with PARDISO, Futur. Gener. Comput. Syst. 20 (3) (2004) 475–487.

[44] P. Wriggers, Nonlinear Finite Element Methods, Springer Science & Business Media, 2008.

[45] F. Verbosio, A. De Coninck, D. Kourounis, O. Schenk, Enhancing the scalability of selected inversion factorization algorithms in genomic prediction, J. Comput. Sci. 22 (2017) 99–108.

[46] B. Kamkari, H.J. Amlashi, Numerical simulation and experimental verification of constrained melting of phase change material in inclined rectangular enclosures, Int. Commun. Heat Mass Transf. 88 (2017) 211–219.

[47] F. Xu, J.C. Patterson, C. Lei, Heat transfer through coupled thermal boundary layers induced by a suddenly generated temperature difference, Int. J. Heat Mass Transf. 52 (21–22) (2009) 4966–4975.